Thesis for the Degree of Doctor of Philosophy

Modelling and Retrieval of Forest Parameters from Synthetic Aperture Radar Data

Maciej Jerzy Soja

CHALMERS

Department of Earth and Space Sciences
Chalmers University of Technology
Gothenburg, Sweden 2014

Modelling and Retrieval of Forest Parameters from Synthetic Aperture Radar Data

Maciej Jerzy Soja

ISBN 978-91-7597-076-9

Doktorsavhandlingar vid Chalmers Tekniska Högskola
Ny serie nr 3757
ISSN 0346-718X

Radar Remote Sensing Group
Department of Earth and Space Sciences
Chalmers University of Technology
SE–412 96 Gothenburg, Sweden
Phone: +46 (0) 31 772 1000

Cover: Four images showing the same part of the Remningstorp test site, situated in southern Sweden, in the province of Västergötland, approximately 150 km north-east from Gothenburg. The topmost image is an aerial photograph, provided by the Swedish Land Survey (Lantmäteriet). The second image from the top shows forest height estimate Δh, obtained from two-level model inversion of a VV-polarised TanDEM-X acquisition from 2011-06-04 (incidence angle: 41°, height-of-ambiguity: 49 m), provided by the German Aerospace Center (DLR). The third image from the top shows the canopy density estimate η_0, also obtained from two-level model inversion. Finally, the bottom image shows a biomass estimate obtained from Δh and η_0. The root-mean-square errors are roughly 10% for forest height and canopy density estimates (compared to airborne lidar scanning data), and approximately 15% for the biomass (compared to *in situ* measurement-based biomass estimates). Note that lakes have been masked out. The legends are shown below.

Printed by Chalmers Reproservice
Chalmers University of Technology
Gothenburg, Sweden 2014

to my mom, my siblings, and Monika

Modelling and Retrieval of Forest Parameters from Synthetic Aperture Radar Data

Maciej Jerzy Soja
Department of Earth and Space Sciences
Chalmers University of Technology

Abstract: Frequent, high-resolution mapping of national and global forest resources is needed for improved climate modelling, degradation and deforestation detection, natural disaster management, as well as commercial forestry. Synthetic aperture radar (SAR) is an active radio- or microwave-frequency imaging sensor, which can be optimised to fit specific needs through the choice of the centre frequency. In particular, P-band SAR, with wavelengths around 70 cm, is a promising tool for biomass mapping due to the high sensitivity to tree trunks, whereas X-band SAR, with wavelengths around 3 cm and larger available bandwidths, is a promising tool for high-resolution mapping of forest canopies.

Papers A and B summarise the results obtained within the feasibility study for the European satellite BIOMASS, which is planned to become the first spaceborne P-band SAR system. In Paper A, a forward model relating relevant forest and system parameters to SAR observables is presented and evaluated. In Paper B, a new model for biomass estimation is proposed, in which the significant influence of topographic and moisture variations is treated using empirical corrections. The new model can be used with the same model parameters in two boreal test sites in Sweden, separated by 720 km, with a root-mean-square error (RMSE) of 22–33% of the mean biomass.

In Papers C, D, and E, X-band SAR data acquired with the twin-satellite, single-pass interferometric system TanDEM-X are studied. Using the principles of across-track interferometry, the position of the scattering centre is estimated from the phase difference between two SAR images. With a high-resolution digital terrain model, the interferometric data are ground-corrected, and the elevation of the scattering centre above ground is determined. In Paper C, boreal forest biomass is estimated for one test site in Sweden from ground-corrected TanDEM-X data using three models with tree canopies represented by a random volume, but with different assumptions of the ground component. The best results, with an averaged RMSE of 16%, are obtained with a model accounting for canopy gaps. Based on this observation, a two-level model (TLM) is introduced, in which forest is modelled as two discrete scattering levels: ground and vegetation, the latter with gaps. In Paper D, it is shown that TLM inversion of single-polarised, ground-corrected TanDEM-X data can provide forest height and canopy density estimates, with RMSE values below 10% for a boreal test site in Sweden. In Paper E, biomass is estimated from the inverted TLM parameters, with an RMSE in the interval 12–19% for eighteen acquisitions from two boreal test sites in Sweden.

Keywords: synthetic aperture radar (SAR), forestry, above-ground biomass, forest height, canopy density, P-band, X-band, BIOMASS, TanDEM-X

Appended Papers

The following papers are the main scientific outcome of this thesis and they have been appended in Part II:

Paper A **M. J. Soja** and L. M. H. Ulander, "Polarimetric-Interferometric Boreal Forest Scattering Model for BIOMASS End-to-End Simulator," *IEEE International Geoscience and Remote Sensing Symposium (IGARSS)*, Quebec City, QC, Canada, 13–18 July 2014, pp. 1061–1064

Paper B **M. J. Soja**, G. Sandberg, and L. M. H. Ulander, "Regression-Based Retrieval of Boreal Forest Biomass in Sloping Terrain using P-band SAR Backscatter Intensity Data," *IEEE Transactions on Geoscience and Remote Sensing*, vol. 51, no. 5, pp. 2646–2665, May 2013

Paper C J. I. H. Askne, J. E. S. Fransson, M. Santoro, **M. J. Soja**, and L. M. H. Ulander, "Model-Based Biomass Estimation of a Hemi-Boreal Forest from Multi-Temporal TanDEM-X Acquisitions," *Remote Sensing*, vol. 5, no. 11, pp. 5574–5597, October 2013

Paper D **M. J. Soja**, H. Persson, and L. M. H. Ulander, "Estimation of Forest Height and Canopy Density from a Single Complex Correlation Coefficient," accepted for publication in *IEEE Geoscience and Remote Sensing Letters*, August 2014

Paper E **M. J. Soja**, H. Persson, and L. M. H. Ulander, "Estimation of Forest Biomass from Two-Level Model Inversion of Single-Pass InSAR Data," submitted to *IEEE Transactions on Geoscience and Remote Sensing*, July 2014

Related Publications

Apart from the appended papers, the author has also contributed to several other publications, including the following reports:

- L. M. H. Ulander, A. Gustavsson, B. Flood, D. Murdin, P. Dubois-Fernandez, X. Depuis, G. Sandberg, **M. J. Soja**, L. E. B. Eriksson, J. E. S. Fransson, J. Holmgren, and J. Wallerman (2011), "BioSAR 2010 Technical Assistance for the Development of Airborne SAR and Geophysical Measurements During the BioSAR 2010 Experiment: Final Report," Technical report, European Space Agency, contract no.: 4000102285/10/NL/JA/ef, `https://earth.esa.int/c/document_library/get_file?folderId=87248&name=DLFE-1322.pdf`.

- ESA (2012), "Report for Mission Selection: Biomass," ESA SP-1324/1 (3 volume series), European Space Agency, Noordwijk, The Netherlands, `http://esamultimedia.esa.int/docs/EarthObservation/SP1324-1_BIOMASSr.pdf`.

- K. Papathanassiou, H. Baltzer, L. E. B. Eriksson, A. Gustavsson, F. Kugler, S. K. Lee, S. Sauer, G. Sandberg, **M. J. Soja**, R. Scheiber, T. Le Toan, L. M. H. Ulander, and L. Villard (2012), "Development of Algorithms for Biomass Retrieval," Technical report, European Space Agency, contract no.: 4200023081/NL/AF.

Preface & Acknowledgements

The story of Rapa Nui, or the Easter Island, is probably as interesting as it is tragic. Once an idyllic island in the Pacific, unknown to humanity and almost entirely covered by a palm forest inhabited by several endemic bird species, the arrival of the first Polynesian settlers around 1200 AD[1] drastically changed its landscape. Trees were felled, to be used as fuel, construction material for shelters and boats, and to give land for agriculture. The population of the island grew rapidly, perhaps even beyond ten thousand inhabitants. 887 monolithic statues, called moai and weighing up to 90 tonnes each, were raised. Soon, the lack of forests caused soil erosion and the leaching of agricultural fields, and almost all animals disappeared from the island. The lack of wood made it impossible to build boats for fishing or for fleeing. Hunger struck the islanders; the misery drew them to wars, and possibly also cannibalism[2]. By the arrival of James Cook in 1774, the population of the now barren island was below a thousand people, surrounded by almost equally many gigantic stone sculptures raised by their ancestors.

Although the understanding of our ecosystems has increased significantly since the arrival of the first Polynesians on Rapa Nui, deforestation and degradation of forests are still a clear and present danger to the entire global ecosystem. Moreover, due to the vastness and diversity of the global forests, many forests remain unexplored, making it difficult to study the terrestrial ecosystems.

This doctoral thesis is focussed on synthetic aperture radar (SAR) remote sensing of forests. SAR is a promising tool for frequent, global, high-resolution mapping of forest resources, and it can be used both to improve the knowledge of the global forest

[1] T. L. Hunt and C. P. Lipo, "Late colonization of Easter Island," *Science*, vol. 311, no. 5767, pp. 1603–1606, 2006

[2] P. Rainbird, "A message for our future? The Rapa Nui (Easter Island) ecodisaster and Pacific island environments," *World Archaeology*, vol. 33, no. 3, pp. 436–451, 2002

resources and to enforce international anti-deforestation agreements. It is my goal for this thesis to bring new knowledge to the field of SAR remote sensing of forests and, in the long run, help to better understand and protect our precious forests.

All research is collective, and also this work would not have been possible without the help and support of many fantastic people. In the next few paragraphs, I would like to thank them for their efforts and contributions.

First, I would like to show my deepest gratitude to my main supervisor and mentor, Lars Ulander, for his trust in me and guidance throughout these five years. Under his watchful eye, I was able to write a couple of articles and a thesis of which I am very proud of. It is a rare gift to be both a good supervisor and a knowledgeable researcher, and Lars is both.

Also, I would like to thank Gustaf Sandberg, my colleague, fellow doctoral student, and co-author of several papers, for the countless discussions, support, inspiration, and cooperation. Gustaf introduced me to the field of remote sensing through the supervision of my bachelor thesis, and, later, he introduced me to radar remote sensing, through the supervision of my master thesis. Thanks to Gustaf, I have been able to find the fascinating field of SAR remote sensing.

I would like to thank my co-supervisors: Leif Eriksson, for his tireless work as the head of the Radar Remote Sensing Group, and Johan Fransson from the Swedish University of Agricultural Sciences (SLU) in Umeå, for his expertise on forest matters. Likewise, I owe a lot of thanks to Jan Askne and Henrik Persson, my co-authors and discussion partners.

I would also like to thank Anders Berg, for being a superb colleague and the perfect room-mate at work. Additionally, I would like to acknowledge my other colleagues from the group and from the Department of Earth and Space Sciences, for making it a pleasant working environment, especially: Gisela Carvajal, Jan Torgrimsson, Malin Johansson, Erik Blomberg, Marston Johnston, Mattias Andersson, Johan Löfgren, Donal Murtagh, the administrative staff, as well as Jo Urban, whose sudden passing struck us all with great sorrow.

Special thanks to Swedish National Space Board (SNSB), European Space Agency (ESA), and European Union (EU) for the funding of my work. I would also like to thank my colleagues from the BIOMASS feasibility study group, other colleagues from SLU, FOI, DLR, as well as anonymous reviewers and committees whose work contributed to this thesis.

I would like to express my gratitude to all the good teachers at Chalmers, for actually teaching me something, and all the other teachers, for helping me to choose what not to study. Many thanks to Conny Modig, my high school physics and maths teacher at Västerhöjdsgymnasiet in Skövde, for making physics fun. Additional thanks to my primary school maths and science teachers in Warsaw, Poland, for force-feeding me with knowledge in such abundance, that I was able to focus my first school years in Sweden on Swedish and English, rather than physics and maths.

Last, but absolutely not least, I would like to thank my family and my closest friends for your love, support, and patience. Special thanks to my mom Małgorzata, for being my role model, my cool siblings Kasia, Jan, and Paweł, for all the laughs we have together, and my dearest Monika, for coming into my life when I needed you the most, with all your happiness and joy. I am looking forward to our future adventures together!

Maciej Jerzy Soja
June 20th, 2014

Credits

The panorama of Rapa Nui on page ix is an adapted version of the photo "Rano Raraku quarry" (http://commons.wikimedia.org/wiki/File:Rano_Raraku_quarry.jpg) by Wikimedia contributor Rivi, available under the license Creative Commons Attribution-Share Alike 3.0 Unported (http://creativecommons.org/licenses/by-sa/3.0/). All other graphics in this thesis are the author's original work.

- TanDEM-X and TerraSAR-X data have been provided by the German Aerospace Center (DLR) within proposal XTI_VEGE0376.
- BioSAR 2007, 2008, and 2010 data have been provided by the European Space Agency (ESA).
- Aerial photographs and lidar digital terrain models (DTMs) have been provided by the Swedish Land Survey (Lantmäteriet).
- Reference forest data have been provided by the Swedish University of Agricultural Sciences (SLU).
- Meteorological data have been provided by the Swedish Meteorological and Hydrological Institute (SMHI).

Contents

I Introduction **1**

List of Abbreviations 3

Chapter 1 – Forests 5
- 1.1 Multiple Roles of Forests . . . 5
- 1.2 Synthetic Aperture Radar in Forestry . . . 6
  - 1.2.1 P-band . . . 7
  - 1.2.2 X-band . . . 8
- 1.3 Thesis Scope and Structure . . . 10

Chapter 2 – Synthetic Aperture Radar 11
- 2.1 1D: Radar Basics . . . 11
  - 2.1.1 Range Measurements . . . 13
  - 2.1.2 Power Measurements . . . 14
  - 2.1.3 Velocity Measurements . . . 14
- 2.2 2D: Synthetic Aperture Radar (SAR) . . . 14
  - 2.2.1 SAR Image Formation . . . 15
  - 2.2.2 SAR Image Processing . . . 17
  - 2.2.3 SAR Image Properties . . . 19
- 2.3 3D: Advanced SAR Techniques . . . 22
  - 2.3.1 SAR Polarimetry . . . 23
  - 2.3.2 SAR Interferometry . . . 26
- 2.4 Past, Present, and Future SAR Systems . . . 32
  - 2.4.1 PolSAR Systems . . . 32
  - 2.4.2 InSAR Systems and Satellite Constellations . . . 33

Chapter 3 – Microwave Scattering from Forests 35
- 3.1 Basic Scattering Mechanisms . . . 36
  - 3.1.1 Direct Backscatter . . . 36
  - 3.1.2 Double-Bounce Interactions . . . 39
  - 3.1.3 Dominant Mechanisms at P- and X-bands . . . 40
- 3.2 Models for Forest Scattering . . . 41
  - 3.2.1 Empirical Models . . . 41
  - 3.2.2 Theoretical Models . . . 42

Chapter 4 – Summary of the Appended Papers 45
- 4.1 Experimental Data . . . 45

4.2 Paper A 47
4.3 Paper B 49
4.4 Paper C 51
4.5 Paper D 53
4.6 Paper E 55

Chapter 5 – Conclusions 59
5.1 Thesis Highlights 60
5.2 Future Prospects 60

References 63

II Appended Papers 79

Paper A 81

Paper B 87

Paper C 109

Paper D 135

Paper E 143

Part I

Introduction

List of Abbreviations

ALS	airborne lidar scanning
ASI	Italian Space Agency (*Italian:* Agenzia Spaziale Italiana)
ATI	along-track interferometry
BEES	BIOMASS End-to-End Simulator
CARABAS	Coherent All RAdio BAnd Sensing
CAST	Chinese Academy of Science and Technology
CDTI	Centre for the Development of Industrial Technology (*Spanish:* Centro para el Desarrollo Tecnologico Industrial)
CONAE	National Commision for Space Activities (*Spanish:* COmisión Nacional de Actividades Espaciales)
COSMO-SkyMed	COnstellation of Small satellites for the Mediterranean basin Observation
CSA	Canadian Space Agency
dbh	diameter at breast height
DCM	digital canopy model
DEM	digital elevation model
DLR	German Aerospace Center (*German:* Deutsches Zentrum für Luft- und Raumfahrt)
DSM	digital surface model
DTM	digital terrain model
EM	electromagnetic
ERS	European Remote Sensing satellite
ESA	European Space Agency
E-SAR	Experimental-SAR
FM	forward model
FOI	Swedish Defense Research Agency (*Swedish:* Totalförsvarets Forskningsinstitut)
GOM	geometrical optics model
HH	horizontal (receive), horizontal (transmit)
HOA	height-of-ambiguity
HV	horizontal (receive), vertical (transmit)
IEEE	Institute of Electrical and Electronics Engineers
InSAR	interferometric SAR

ISRO	Indian Space Research Organisation
ITU	International Telecommunication Union
IWCM	interferometric water cloud model
JAXA	Japan Aerospace Exploration Agency
lidar	light detection and ranging
NASA	National Aeronautics and Space Administration
PD	penetration depth
pdf	probability distribution function
PolInSAR	polarimetric-interferometric SAR
PolSAR	polarimetric SAR
radar	radio detection and ranging
RCS	radar cross section
RISAT	Radar Imaging Satellite
RMSD	root-mean-square difference
RMSE	root-mean-square error
RVoG	random volume over ground
SAR	synthetic aperture radar
SLU	Swedish University of Agricultural Sciences (*Swedish:* Sveriges lantbruksuniversitet)
SMHI	Swedish Meteorological and Hydrological Institute (*Swedish:* Sveriges Meteorologiska och Hydrologiska Institut)
SNR	signal-to-noise ratio
SPM	small perturbation model
SRTM	Shuttle Radar Tomography Mission
TanDEM-X	TerraSAR-X Add-oN for Digital Elevation Measurements
TBM	TLM biomass model
TDM	TanDEM-X (interferometer system)
TDX	TanDEM-X (satellite)
TLM	two-level model
TOPS	terrain observation by progressive scans
TSX	TerraSAR-X (satellite)
UHF	ultra high frequency
VH	vertical (receive), horizontal (transmit)
VHF	very high frequency
VV	vertical (receive), vertical (transmit)
XTI	across-track interferometry

Chapter 1

Forests

1.1 Multiple Roles of Forests

Forests play a vital role in the terrestrial ecosystems. Through the process of photosynthesis, trees and plants bind CO_2 from the atmosphere, part of which is transformed into carbon stock. Forests provide shelter to countless animal and vegetation species, housing around 80% of the terrestrial biodiversity [1]. They also take part in the water cycle, prevent soil from erosion, and clean water and air from pollutants. At the same time, forests are one of our greatest natural resources. Timber is used as a construction material, for paper production, and as a fuel. Animals and vegetation provide food. Also, forests have great recreational values.

For a long time, the global effects of human exploitation of forests were negligible due to the relatively small population and ineffective harvesting methods. However, during the last few centuries, the rapid growth of the human population caused an increased demand on forest products, which together with the excessive use of fossil fuels started to more significantly affect the global environment. In the second half of the 20th century, the signs of human influence on the global ecosystem could be observed, for example in the form of acid rains, ozone depletion, and probably also global warming. Although the public awareness of the environmental issues has increased during the last few decades and the first measures have been taken, there is still much to be learnt, and a lot of research is focussed on Earth system science

and climate change.

One of the greatest concerns is the influence of deforestation on global CO_2 emissions. Some sources state, that as much as 20% of the global CO_2 emissions come from deforestation [2], but the exact numbers are unknown. One of the largest uncertainties in the current carbon cycle models is introduced by the inaccurate estimates of the terrestrial carbon stocks and fluxes, mainly associated with forests. The most relevant, measurable quantity directly related to the carbon distribution in the biosphere is biomass, which is the total dry mass of all organic tissue. Since roughly 50% of biomass is carbon, and forests account for around 80% of the terrestrial above-ground biomass [3], frequent and global mapping of forest biomass is needed for improved carbon cycle modelling and climate change prediction. High-resolution mapping of biomass and other forest parameters, e.g., forest height and canopy density, will also aid the detection of deforestation and forest degradation, improve natural disaster handling, and enable efficient and sustainable management in commercial forestry.

1.2 Synthetic Aperture Radar in Forestry

Forests cover more than 31% of the total land surface of the Earth [1], and spaceborne remote sensing is the only feasible method for frequent and global mapping of forests [3]. There are several different spaceborne remote sensing techniques which can be used for forest mapping. Optical methods have long been used for this task. However, these methods are sensitive to atmospheric conditions, which is especially problematic for the high-biomass tropical rainforests around the equator, where the cloud cover is the most persistent [3]. Airborne lidar scanning (ALS) is currently considered the most accurate remote sensing method for forest mapping [4]. However, spaceborne application of this technique is difficult, due to yet unresolved resolution, coverage, and technology limitations [3].

Synthetic aperture radar (SAR) does not suffer from the same disadvantages as the optical and lidar sensors. As an active radio- or microwave-frequency sensor, it provides its own illumination and it is generally less sensitive to clouds than the optical methods. Thanks to the synthetic aperture technique, the image resolution of a spaceborne SAR system can be of the order of metres. SAR is one of the most promising tools for forest remote sensing and many past and ongoing studies are dedicated to forest parameter estimation from SAR data [5]. A comprehensible introduction to SAR can be found in [6].

As the electromagnetic waves scatter more strongly from objects of sizes comparable to, or larger than the wavelength, SAR systems can be optimised to fit specific needs through the choice of the centre frequency [7], and they are commonly classified by the used frequency band. Two frequency bands often used for spaceborne SAR imaging of forests are the P- and X-bands. At P-band, the wavelength is around 70 centimetres and the strongest scatterers are large branches and tree trunks, which also contain most of the biomass. This causes the scattering centre to be located in the lower part of the canopy. At X-band, the wavelength is around 3 centimetres and

scattering occurs even from the smaller branches, leaves, and needles in tree canopies. Therefore, the penetration capabilities are significantly lower than at P-band, and the scattering centre is located closer to the canopy top.

1.2.1 P-band

Many studies of VHF-band (30–300 MHz) data acquired with the Swedish SAR systems CARABAS-I and -II (20–90 MHz) have shown the excellent potential of VHF-band SAR for stem volume mapping [8–22], and, since stem volume is highly correlated with biomass, these conclusions also apply to biomass mapping. However, VHF-band SAR is not available for spaceborne use, primarily due to the large ionospheric distortions and lack of suitable frequency allocations [23].

A somewhat higher frequency band is the P-band (typically 420–450 MHz), for which numerous studies have shown good correlation between the backscattered signal strength and biomass over a wide biomass range [24–40]. It has also been shown that the temporal stability is high at P-band [41–43], making it possible to perform repeat-pass interferometry and tomography with a single satellite [41, 44–48]. This is an important result, as the interferometric and tomographic data may enable the estimation of forest height and the horizontal and vertical forest structure, which may both improve biomass estimation and provide other important forest parameters. Moreover, spaceborne signal transmission at P-band is since 2003 allowed for secondary use within a 6-MHz sub-band with a centre frequency of 435 MHz, and the ionospheric disturbances have been shown to be manageable [3, 49, 50].

In 2013, the European Space Agency (ESA) selected BIOMASS for the 7th Earth Explorer mission [51]. BIOMASS will be the first spaceborne P-band SAR system, designed to provide global biomass, biomass change, and forest height maps. The launch of BIOMASS is currently scheduled for 2020.

To be able to assess the error budget of the future BIOMASS mission, an end-to-end simulator has been implemented [52]. In the simulator, the processing chain of the satellite is modelled, including explicit error sources. Retrieval algorithms are applied to the modelled SAR data, and biomass estimation errors are studied against system parameters. An essential part of the entire simulator is the forward model, which generates the raw reflectivity data.

- In Paper A, a polarimetric-interferometric forward model used within the BIOMASS end-to-end simulator (BEES) is developed and evaluated for SAR image generation in boreal forest. The model predicts the extended covariance matrix from relevant forest and system parameters. It is a hybrid model, in which the polarimetric matrix is modelled with empirical relations, whereas the interferometric matrix is modelled using a theoretical model.

One of the difficulties at P-band is the significant influence of topographic and moisture variations on the backscattered signal. There is a need for a biomass retrieval model which accounts for the influence of these effects, and which can be used on large

scales without requiring excessive training data. In the past studies, the proposed models have often been developed and evaluated using small amounts of experimental data, usually limited to acquisitions made in similar conditions over one single test site.

- In Paper B, a new biomass retrieval model is proposed. The model features empirical correction terms, which compensate for the influence of topographic and moisture variations. The model is compared to five other models, and evaluated using airborne SAR data acquired in different seasons and at different flight headings over two boreal test sites in Sweden separated by 720 km. It is concluded that the proposed model performs significantly better than the other models, and it can be successfully used in both test sites with the same model parameters.

1.2.2 X-band

Currently, the highest frequency allocations used for spaceborne SAR imaging of the Earth are located within the X-band (8–12 GHz). As mentioned earlier, the scattering centre is located in the upper part of the canopy, and the principles of SAR interferometry (InSAR) can be used to map the canopy height from small phase differences between two SAR images acquired at slightly different incidence angles [53, 54].

The TanDEM-X system, developed and operated by the German Aerospace Center (DLR), is an X-band SAR interferometer consisting of two almost identical satellites in a tight tandem formation [55]. Its primary goal is to provide the first global, high-resolution digital elevation model (DEM), which will replace the older DEM produced from the data acquired in February 2000 during the Shuttle Radar Topography Mission (SRTM) [56]. With the tight tandem formation, the temporal decorrelation is negligible for most land surfaces [55], and precise DEM estimation can be done even for the dynamic tree canopies.

One of the first models developed for forest parameter estimation from InSAR data is the interferometric water cloud model (IWCM), originally designed for stem volume estimation from multi-temporal, repeat-pass InSAR data acquired with the C-band systems ERS-1/2 [57, 58]. In the IWCM, forest canopy is modelled as a random volume with canopy gaps. To account for the temporal changes occurring between the two interferometric acquisitions, temporal decorrelation is modelled, separately for the ground and volume contributions. Model agreement with observations is achieved through the inclusion of empirical relations between stem volume and forest height, and between stem volume and backscatter intensity.

In the traditional use of the IWCM with single-polarised, single-baseline data, the number of model parameters is larger than the number of available observables. Therefore, model parameters are treated as constants for each acquisition, and estimated from training data. Using multi-temporal data, the influence of the acquisition geometry and environmental variables on model parameters can be studied, and biomass estimation algorithms can be developed.

- In Paper C, biomass is estimated from multi-temporal TanDEM-X acquisitions using the IWCM and two simpler models, one neglecting canopy gaps and one neglecting both canopy gaps and ground contribution. Model training and validation are conducted on two separate data sets. It is concluded that the most accurate biomass prediction can be achieved with the IWCM, i.e., when both canopy gaps and the ground contribution are modelled, and for InSAR data with large interferometric baselines.

The acquisition of training data is generally laborious and expensive, and, from the operational point of view, it is beneficial to decrease the requirements on field inventories. The random volume over ground (RVoG) model can be seen as a simplified version of the IWCM, with neglected canopy gaps and no temporal decorrelation modelling [59, 60]. Direct inversion of the RVoG model has been shown useful for the estimation of forest height and ground topography from interferometric and fully polarimetric, L- and P-band SAR data, without the need for model training [45, 60, 61]. For the standard, single-polarised TanDEM-X image pairs acquired within the global mapping campaign, direct inversion of the RVoG model requires further simplifications, to balance the number of parameters with the number of observables [62, 63].

By using an external, high-resolution digital terrain model (DTM), the number of model parameters can be reduced. With the general stability of the ground surface in forested areas, the increasing availability of DTMs acquired within national lidar scanning campaigns, as well as the future P- and L-band (1–2 GHz) InSAR missions (BIOMASS, and possibly also SAOCOM-CS [64] and TanDEM-L [65]), the availability of high-resolution DTMs will increase in time, making this approach useful from an operational point of view.

At X-band, canopy openings are often large in comparison to the wavelength, and the effective attenuation in the canopies is significant. It is therefore motivated to allow penetration to occur only through canopy gaps. This results in a two-level model, in which forest is represented by two discrete scattering levels, with their relative contributions to the total backscattered field determined by the canopy closure. With an external DTM, direct inversion of this two-level model is feasible even for the single-polarised case, and estimates of both forest height and canopy density may be obtained. This may also lead to improved biomass estimation performance.

- In Paper D, it is observed that the ground-level contribution is significant in boreal forests at X-band. Based on that observation, an interferometric two-level model (TLM) is introduced, in which penetration through forest canopy can occur only through canopy gaps. The model has a simple form and can be inverted if a high-resolution DTM is available, without the need for multiple SAR acquisitions. It is shown that TLM inversion provides accurate estimates of both forest height and canopy density.

- In Paper E, estimates of forest height and canopy density obtained from the TLM inversion described in Paper D are used as biomass predictors. The new model

is evaluated on experimental data from two boreal test sites in Sweden. It is concluded that the model performance is excellent within each test site (in fact, close to that achievable with ALS data). However, similarly to the case of ALS-based mapping, the same model parameters cannot be used in both test sites, due to the significant differences in the structure of forest canopies in the two test sites.

1.3 Thesis Scope and Structure

The main scope of this thesis is to develop methods for forest parameter estimation from SAR. At P-band, focus is put on the influence of topographic and moisture variations on biomass retrieval from SAR intensity data, in view of the future BIOMASS mission. At X-band, focus is put on the influence of the canopy gaps on scattering and the potential of X-band InSAR for large-scale mapping of forest height, canopy density, and biomass, for example with the existing global TanDEM-X data.

This thesis consists of two main parts: **Part I**, in which the motivation for this thesis has been given in this chapter, the basics of SAR are presented in the next chapter (Chapter 2), scattering from forests is studied in Chapter 3, the appended papers are summarised in Chapter 4, and some final conclusions and future prospects are presented in Chapter 5, and **Part II**, containing the appended papers, which are the main scientific outcome of this thesis.

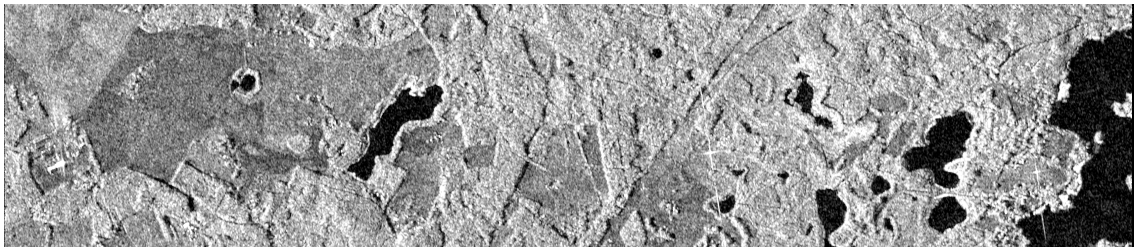

Chapter 2

Synthetic Aperture Radar

In this chapter, synthetic aperture radar is introduced. First, the principles of the basic, one-dimensional radar measurements are presented. Thereafter, a second dimension is added, and high-resolution radar imaging is introduced. Lastly, more advanced techniques, expanding radar imaging capabilities beyond two dimensions, are presented.

2.1 1D: Radar Basics

Radar is an active remote sensing technique in which electromagnetic (EM) signals are transmitted, and the reflected echoes are detected, processed, and analysed [67–69]. The principles of radar are similar to the principles of echolocation, which is an ultrasonic navigation technique used by bats and toothed whales. Since radar is an active system, no external illumination is needed. Also, the terrestrial atmosphere is almost transparent to EM waves with frequencies up to approximately 10 GHz, meaning that radar systems can see through clouds [68, 70, 71]. Note, however, that the influence of the ionosphere increases with decreasing frequency, thus effectively reducing the potential usefulness of frequencies below a few hundred MHz for spaceborne radar [3, 71].

Although the development of radar-like systems started already in the beginning of the 20th century, it was first in 1940 that the term "radar" was introduced by

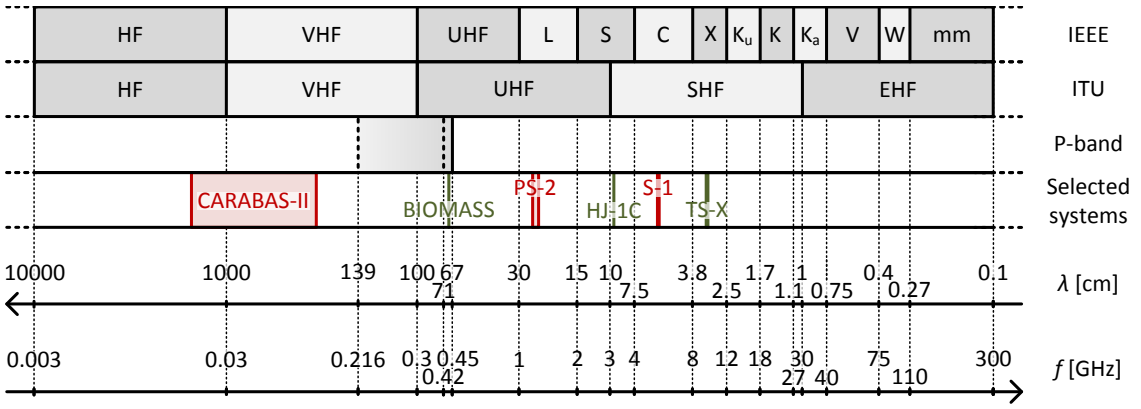

Figure 2.1: Radar frequency bands according to the IEEE and ITU standards. Logarithmic scales are used for frequency f and wavelength λ. Commonly, P-band is defined as the interval 420–450 MHz, but the broader interval 216–450 MHz can also be encountered in the literature. Frequency bands used by some selected SAR systems are also shown. CARABAS-II was an airborne system from the Swedish Defence Research Agency (FOI) [66]. The European BIOMASS satellite is planned to be the first P-band SAR in space, whereas the Japanese ALOS-2 PALSAR-2 (PS-2), Chinese HJ-1C, European Sentinel-1 (S-1), and German TerraSAR-X (TS-X) are examples of current spaceborne L-, S-, C-, and X-band SAR systems, respectively, see Section 2.4.

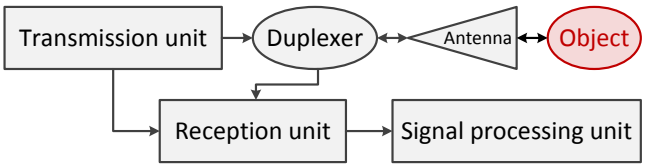

Figure 2.2: Typical setup for a monostatic radar system.

the US Navy, as an abbreviation for "*ra*dio *d*etection *a*nd *r*anging" [72, 73]. Modern radar systems are capable of not only detection and ranging, but also velocity measurements, shape and size determination of objects, angular measurements, and multi-dimensional mapping, and their applications include parking assistance in cars, traffic speed monitoring, airport surveillance, rain rate and wind mapping for weather forecasting, aircraft guidance and detection, planetary mapping from satellites, and space object monitoring from the ground [67, 68].

Since the scattering properties of objects are dependent on the frequency of the transmitted EM waves, the choice of the centre frequency determines the area of ap-

plication of a radar system. To simplify the classification of radar systems, frequency bands have been introduced [67]. There are two main standards, one defined by the Institute of Electrical and Electronics Engineers (IEEE) and one by the International Telecommunication Union (ITU), and both nomenclatures are summarised in Figure 2.1. Although still used by the radar community, the P-band is an old band designation and it has been replaced by the UHF-band. P-band is commonly defined as the interval 420–450 MHz, although the broader interval 216–450 MHz can also be encountered in the literature [74, 75].

A radar system in which both transmission and reception are done from the same position is called monostatic. In case of multiple positions, the system is called multistatic (or bistatic in the case of two positions). The typical setup for a monostatic radar system is schematically depicted in Figure 2.2. In the transmission unit, an EM signal with the desired waveform and power is generated. The signal is then directed towards the antenna via a duplexer, which often is a switching device, alternating the functions of the radar unit between transmission and reception. The antenna transmits a wave into a medium (usually air), the wave is scattered from an object, and an echo is registered back at the antenna. The received signal passes again through the duplexer, which now guides it towards the reception unit. In the reception unit, the received signal is processed, sampled, and transmitted to a digital signal processing unit.

2.1.1 Range Measurements

The distance between the target and the antenna is called range and it can be estimated from the time delay between the signal transmission and the reception of the echo. If this time delay is denoted T, then the corresponding range is [76]:

$$R = \frac{cT}{2}, \tag{2.1}$$

where a factor of 2 accounts for the two-way propagation and c is the propagation velocity of the EM waves in the medium. In most radar applications, the latter is air and $c = c_0$ is often assumed, where c_0 is the speed of light in vacuum.

In the simplest radar systems, bursts of monochromatic EM waves are transmitted, and the best achievable range resolution is proportional to the pulse length [68]:

$$\delta_R = \frac{c\tau}{2}. \tag{2.2}$$

Thus, fine resolution can be achieved with short pulses, which decreases the signal-to-noise ratio (SNR) and aggravates signal detection. To avoid this problem, most modern radar systems use coded pulses with bandwidth B. For such systems, the best achievable range resolution is [68]:

$$\delta_R = \frac{c}{2B}. \tag{2.3}$$

The resolution is now inversely proportional to the signal bandwidth, and both fine resolution and high SNR can be achieved simultaneously.

2.1.2 Power Measurements

The signal-to-noise ratio (SNR) is a useful benchmark for system quality. The SNR is the ratio between the received signal energy and the noise power density, and for a monostatic system using coherent integration of multiple pulses, it is determined by [68]:

$$\mathrm{SNR} = \frac{P_{\mathrm{avg}} \lambda^2 G^2 t_{\mathrm{dwell}} \sigma}{(4\pi)^3 R^4 L C_B k_B T_s}, \tag{2.4}$$

where P_{avg} is the average power transmitted by the system during the dwell time (integration time) t_{dwell}, λ is the wavelength, G is the antenna gain, R is the range, L is a factor representing losses, C_B is the filter mismatch factor ($C_B = 1$ for a perfectly matched filter), k_B is Boltzmann's constant, T_s is the system noise temperature, and σ is the radar cross section (RCS). The RCS is the main observable in a radar system and it is the effective cross-section area of the target, measured in square metres. The RCS depends not only on the EM properties and the shape of the target, but also on system parameters such as polarisation, angle of incidence, and frequency.

2.1.3 Velocity Measurements

If a scatterer positioned within the antenna beam is moving radially relative the antenna, a frequency shift known as the Doppler shift will occur. The Doppler shift f_D can be computed using [68]:

$$f_D = -\frac{2\dot{R}(t)}{\lambda}, \tag{2.5}$$

where

$$\dot{R} = \frac{\mathrm{d}R(t)}{\mathrm{d}t} \tag{2.6}$$

is the radial velocity of the scatterer.

2.2 2D: Synthetic Aperture Radar (SAR)

Radar imaging can be achieved by sweeping the radar antenna, for example by mounting it in a side-looking configuration on an airborne- or spaceborne-platform. The target position is then determined by its range and by the along-track position of the antenna. Commonly, these two dimensions are referred to as slant range and azimuth, whereas the projected ground distance to the scatterer is called ground range. These concepts are illustrated in Figure 2.3.

For a radar antenna with along-track aperture size D_x such that:

$$D_x \gg \lambda, \tag{2.7}$$

the beamwidth is approximately [68]:

$$\Delta\phi \approx \frac{\lambda}{D_x}, \tag{2.8}$$

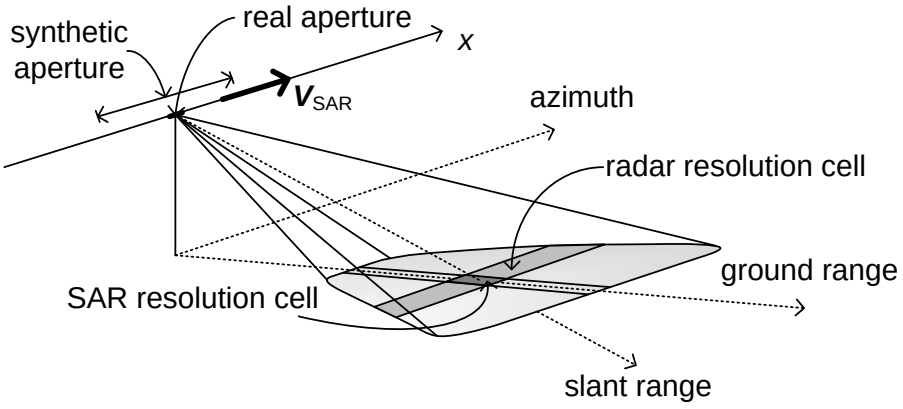

Figure 2.3: Basic imaging radar geometry under flat-earth approximation.

and the azimuth resolution at range R can be approximated by [68]:

$$\delta_x \approx \Delta\phi R \approx \frac{\lambda R}{D_x}. \tag{2.9}$$

As it can be observed in (2.9), the azimuth resolution is proportional to range and inversely proportional to the antenna aperture. Fine azimuth resolution therefore requires large antennas, which is both impractical and expensive, especially in the spaceborne case, for which a moderate resolution of 100 m at X-band would require an antenna with an aperture size of a few hundred metres.

Synthetic aperture radar (SAR) presents a solution to the aforementioned resolution problem. Through coherent signal processing, a larger, synthetic aperture can be created using the phase information from several consecutive pulse echoes.

This technique was first proposed in the early 50's, and further developed during the decades that followed [67]. In 1978, the first civilian, spaceborne SAR system called Seasat was launched by NASA [77], and in the early 90s, Europe (ESA), Russia, Japan, and Canada followed with their own systems. In the early 2000s, additional SAR satellites were launched by countries such as Germany, Italy, India, China, and South Korea, and both Spain and Argentina are planning to launch their first systems within a few years. Presently, more than 15 civilian SAR satellites are operating and around 10 are planned to be launched within the forthcoming five years [6, 78].

2.2.1 SAR Image Formation

The main concept of SAR is to synthesise a large antenna using multiple pulse echoes received by a smaller antenna moving along a known path [76,79]. From (2.9), a small

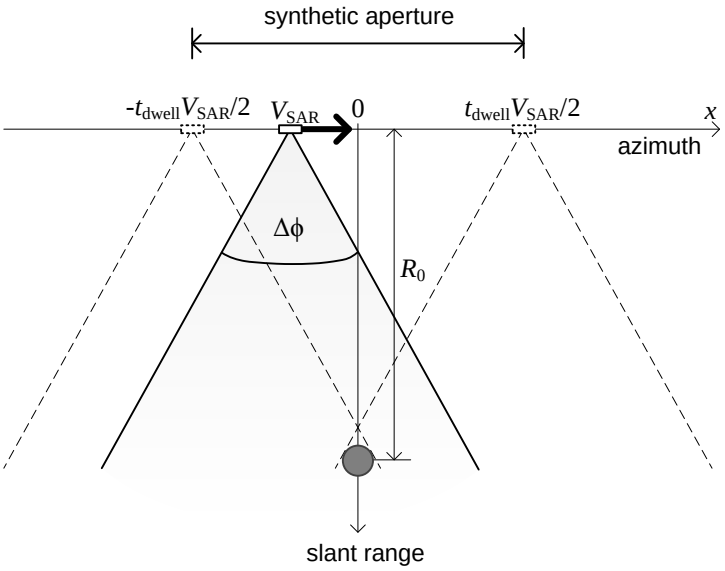

Figure 2.4: Basic slant range plane geometry of SAR.

radar antenna has a large footprint. An arbitrary scatterer on the ground is then covered by several consecutive pulse echoes received at different azimuth positions, and the relative radial velocity $\dot{R}$ of that scatterer is different at each azimuth position. Therefore, the Doppler shift induced by the relative motion of the scatterer changes with azimuth, creating a Doppler bandwidth. With coherent signal processing, azimuth resolution can be improved in the same way as range resolution is improved using coded pulses.

Assume that a radar antenna is travelling along the x-axis on a straight path with velocity V_{SAR}, according to the simplified geometry shown in Figure 2.4. Let R_0 be the range of closest approach to an arbitrary scatterer, and let t be the azimuth time such that $t = t_0 = 0$ is the time of closest approach. The instantaneous distance between the radar antenna and the scatterer can be computed using the Pythagorean theorem:

$$R(t) = \sqrt{R_0^2 + (V_{\mathrm{SAR}}t)^2} \approx R_0 \left(1 + \frac{(V_{\mathrm{SAR}}t)^2}{2R_0^2}\right), \tag{2.10}$$

where a Taylor expansion has been used under the assumption that $V_{\mathrm{SAR}}t \ll R_0$.

The radial velocity of the scatterer relative the antenna can be computed from (2.10):

$$\dot{R}(t) = \frac{\mathrm{d}R(t)}{\mathrm{d}t} \approx \frac{V_{\mathrm{SAR}}^2 t}{R_0} \tag{2.11}$$

and the corresponding Doppler frequency can be computed using (2.5) and (2.11):

$$f_D(t) = -\frac{2\dot{R}(t)}{\lambda} \approx -\frac{2V_{\text{SAR}}^2 t}{\lambda R_0}. \tag{2.12}$$

For the simplified slant range geometry depicted in Figure 2.4, the integration time can be computed from the antenna footprint in (2.9) and the antenna velocity V_{SAR}:

$$t_{\text{dwell}} \approx \frac{\lambda R_0}{V_{\text{SAR}} D_x}. \tag{2.13}$$

The Doppler bandwidth is the difference between the maximal and minimal Doppler frequencies. It can be computed using (2.12) and (2.13) as:

$$B_D = f_D\left(t_{\text{dwell}}/2\right) - f_D\left(-t_{\text{dwell}}/2\right) \approx \frac{2V_{\text{SAR}}}{D_x}. \tag{2.14}$$

Similar to the range resolution for a coded pulse with bandwidth B, see (2.3), SAR azimuth resolution can be computed from the ratio of the antenna velocity V_{SAR} and the Doppler bandwidth B_D [68]:

$$\delta_x = \frac{V_{\text{SAR}}}{B_D} = \frac{D_x}{2}, \tag{2.15}$$

which means that the azimuth resolution of a SAR image can be as good as half the aperture length of the antenna.

The SAR mode presented above, with fixed antenna direction, is called stripmap SAR [68, 80]. Better resolutions, but lower coverage, can be achieved by focussing the antenna at the same point along the whole synthetic aperture, in a mode called spotlight SAR [68, 79]. A better coverage, but lower resolution, can be achieved by sweeping the antenna in different directions, in modes such as scan SAR and TOPS [68, 81].

Note that there is an essential difference in the way SAR images are resolved as compared to optical imagery. Optical imagery features constant resolution angle in both range and azimuth direction [68]. Far-range pixels are therefore resolved with lower resolution than the near-range pixels. In SAR, pixels are resolved at constant slant-range resolution. When projected to the ground, far-range pixels have better resolution than near-range pixels (assuming flat earth). For spotlight SAR, azimuth resolution is range-dependent, with better resolution achieved in near-range.

2.2.2 SAR Image Processing

The processing of the raw data acquired by a SAR platform can be summarised in three main steps: focussing, radiometric calibration, and geocoding. In the first step, high-resolution images are created. In the second step, pixel values are corrected so that they carry meaningful information. In the third step, the image is re-sampled to a cartographic projection so that it can be easily compared with other types of geographic information.

2.2.2.1 Focussing

Essentially, SAR image focussing consists of a 2D matched filtering, which removes the range and azimuth coding. Using the fast Fourier transform, matched filtering can be performed in the frequency domain at low computational costs. However, one of the main difficulties in frequency-domain processing is range cell migration (RCM), which is the movement of scatterers through resolution cells as the antenna moves along the synthetic aperture [79, 82]. Unless compensated for, the RCM will cause azimuth de-focussing.

In the beginning of digital SAR processing, computational costs were of great concern and many different frequency-domain algorithms have been developed [79,82]. The algorithms differ in the way they deal with the RCM, computational costs, and accuracy.

SAR focussing can also be achieved in the time domain, using back-projection algorithms [83–86]. Time-domain algorithms are generally easier to implement and the errors introduced by the uncertainties in the recorded flight path can often be treated using autofocus techniques. Traditionally, the large computational costs have been a major disadvantage of the time-domain algorithms, but the modern back-projection algorithms, such as the fast-factorised back-projection [86], are both accurate and computationally efficient.

2.2.2.2 Radiometric Calibration

To ensure that the focussed SAR image carries meaningful information, radiometric calibration needs to be performed [76, 87]. In this step, the effects of the range-dependent spreading loss, systematic variation in range due to residual effects of antenna pattern, as well as platform roll and yaw movements (around the velocity vector and the vertical axis, respectively) are treated. Moreover, the influence of system noise and SAR focussing also need to be considered during radiometric calibration.

There are two main approaches to radiometric calibration: internal and external [88, 89]. The internal calibration process is done using pre-flight and in-flight measurements of the effects of each element of the radar system. The external calibration process uses targets with known RCS positioned within the imaged scene, preferably at many different positions [88, 90]. The targets may be active (transmitters) or passive, discrete or distributed. Commonly used passive calibration targets are di- and trihedral corner reflectors, and dense forests.

For the imaging of distributed and dynamic targets, it is useful to average and normalise the measured reflectivity in order to reduce the stochastic variations and to remove the residual range dependence. Scattering coefficient sigma nought is often used for surface imaging, as it removes range-dependence caused by the fact that the resolution cell covers a larger ground area in near-range [91]:

$$\sigma^0 = \frac{\langle \sigma \rangle}{A_{\mathrm{GR}}}, \tag{2.16}$$

where A_{GR} is ground area covered by the resolution cell and $\langle \bullet \rangle$ denotes spatial average. The area A_{GR} can be computed from the slant range area A_{SR} using [92,93]:

$$A_{\mathrm{GR}} = \frac{A_{\mathrm{SR}}}{\cos \psi_i}, \tag{2.17}$$

where ψ_i is the angle between the image plane normal and the ground surface normal.

Scattering coefficient gamma nought is often used for the imaging of volumetric scatterers, as it compensates for the residual range-dependence in σ^0 caused by different penetration depths [94,95]:

$$\gamma^0 = \frac{\sigma^0}{\cos \theta_i}, \tag{2.18}$$

where θ_i is the local angle of incidence.

2.2.2.3 Geocoding

In this step, the focussed SAR image is interpolated from radar geometry to a cartographic projection [70]. A geocoded reference height map is needed, e.g., in the form of a DEM, a geoid model, or an ellipsoid model. From the information about the antenna track, the range and azimuth positions of each pixel in the reference height model can be computed, yielding a geocoding look-up table, which can be used for the interpolation of the focussed image. The look-up table can be fine-tuned using image processing techniques, for example by cross-correlating the focussed intensity image with a synthetic intensity image simulated from a DEM with a simple scattering model.

2.2.3 SAR Image Properties

There are a few effects visible in SAR imagery which need to be considered during image analysis.

2.2.3.1 Geometric Distortions in SAR Images

SAR images are created in a side-looking geometry and they are projections of the three-dimensional world on the two-dimensional range-azimuth plane. Therefore, geometrical distortions and ambiguities are unavoidable. These distortions are especially visible in hilly and mountainous regions, as well as urban areas.

The effect of foreshortening occurs on sloping grounds, where two points, which may be significantly separated in the horizontal direction, appear closer on the radar due to the slope effect, see points A and B in Figure 2.5(a).

In the case of even steeper slopes, or steep incidence angle, the effect of layover may occur and cause the two points to appear in reversed order, as shown in Figure 2.5(b). This means that a mountain peak may sometimes appear closer than a mountain foot.

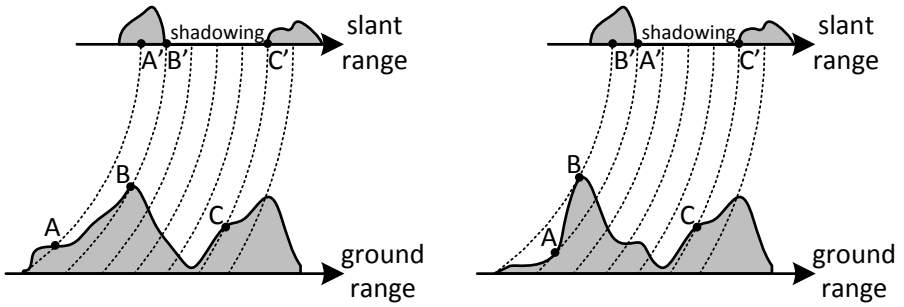

(a) Foreshortening (b) Layover

Figure 2.5: Three geometrical distortions visible in SAR images are here shown schematically. Foreshortening and layover are illustrated by points A and B in (a) and (b), respectively. Shadowing can be seen in (a) between points B' and C' and in (b) between points A' and C'.

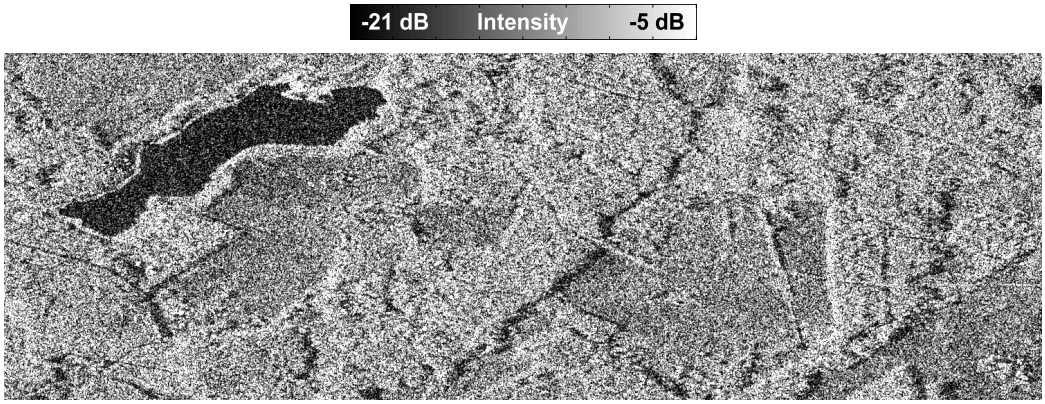

Figure 2.6: A single-look TerraSAR-X intensity image (in dB) over the Remningstorp test site. Speckle is the cause of the grainy texture in the image. Pixel size is 0.9 m in slant range (horizontal direction) and 6.6 m in azimuth (vertical direction), and the image has a size of 1500×500 pixels.

The effect of shadowing occurs when the radar signal is blocked by a large scatterer, e.g., a mountain, and a dark area is visible behind it, like between points B and C in Figure 2.5(a) and Figure 2.5(b).

2.2.3.2 Speckle and SAR Image Statistics

In SAR systems, coherent waves are used for imaging. If there are many scatterers within a resolution cell, interference between the scattered fields may cause an effect

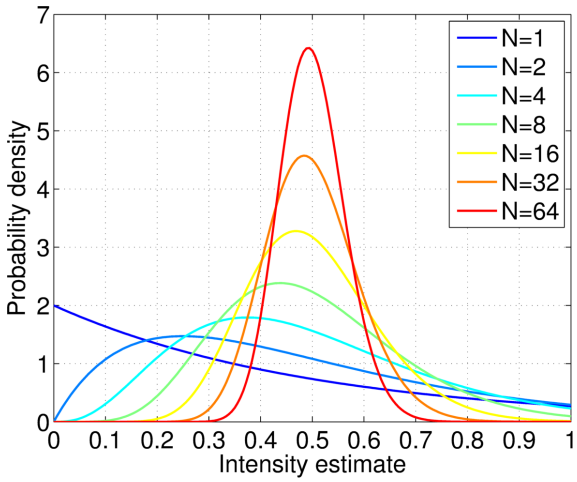

Figure 2.7: Pdf for the N-look RCS estimate $\hat{\sigma}_N$ ($\sigma = 0.5$).

called speckle. Speckle introduces a graininess in SAR images, which deteriorates image quality, see Figure 2.6

Speckle statistics can be studied in the case of fully developed speckle [76, 96], i.e., under the assumption that a resolution cell contains a large number of similar scatterers randomly distributed in range over an extent much larger than the wavelength. The central limit theorem implies that the real and imaginary parts I and Q of the total backscattered field, which is the sum of the individual signals backscattered by each scatterer, are independent, normally distributed random variables with zero mean and variance $\sigma/2$ (where σ is the RCS and the factor of 2 has been chosen to make the total variance equal to σ) [76, 96]. From this follows that the phase is uniformly distributed between $-\pi$ and π, the amplitude $\sqrt{I^2 + Q^2}$ has a Rayleigh probability distribution, and the intensity $\hat{\sigma}_1 = I^2 + Q^2$ has a negative exponential distribution with the following pdf:

$$p(\hat{\sigma}_1|\sigma) = \begin{cases} \frac{1}{\sigma} e^{-\frac{\hat{\sigma}_1}{\sigma}} & \hat{\sigma}_1 \geq 0 \\ 0 & \text{otherwise} \end{cases} . \tag{2.19}$$

As mentioned earlier, speckle appears in SAR imagery as a noise-like pattern, and it is most often an unwanted nuisance, aggravating the performance of segmentation algorithms and general image interpretation. One way to reduce speckle in intensity images is by non-coherent averaging, i.e., multilooking. There are several ways to achieve this: by splitting the range or Doppler spectrum into several parts, processing each part separately, and then averaging the final images; by spatial averaging of intensity (or amplitude, although intensity averaging has been shown superior [88]); or by averaging of several SAR images over the same scene (assuming stable scatterers). With non-coherent averaging, the variance in the image is decreased, but at the cost

of resolution or additional acquisitions. Many studies have been devoted to speckle filtering and there are many different filtering algorithms available [96].

The N-look intensity $\hat{\sigma}_N = \frac{1}{N}\sum_{i=1}^{N}(I_i^2 + Q_i^2)$, where I_i and Q_i are assumed to be independent, normally distributed random variables, is a gamma distributed random variable with the following pdf [76, 96]:

$$p(\hat{\sigma}_N|\sigma, N) = \begin{cases} \frac{N^N \hat{\sigma}_N^{N-1}}{(N-1)!\sigma^N} e^{-\frac{N\hat{\sigma}_N}{\sigma}} & \hat{\sigma}_N \geq 0 \\ 0 & \text{otherwise} \end{cases}. \tag{2.20}$$

In Figure 2.7, the pdf for the N-look intensity estimate $\hat{\sigma}_N$ is plotted for $\sigma = 0.5$. It can be observed that with an increasing number of looks, the distribution becomes more symmetric around the mean, and the variance decreases.

In Figure 2.8, the effect of multilooking is visualised in a simulated SAR image. In Figure 2.8(a) and Figure 2.8(b), the real and imaginary parts are shown. The central part of the image has slightly larger variance, but it can barely be seen. In Figure 2.8(c), the complex phase is shown, and it is completely random. In Figure 2.8(d), the amplitude is shown, and a feature can be observed. In Figures 2.8(e)–2.8(i), the effect of number of looks on the variance is shown. The reference RCS is shown in Figure 2.8(j).

It can be shown that the expectation value and the variance of an N-look intensity estimate are [76, 96]:

$$\mathrm{E}\left[\hat{\sigma}_N\right] = \sigma, \tag{2.21}$$

$$\mathrm{Var}\left[\hat{\sigma}_N\right] = \frac{\sigma^2}{N}. \tag{2.22}$$

The N-look intensity is therefore an unbiased estimate of the RCS, with variance decreasing as $\frac{1}{N}$.

2.3 3D: Advanced SAR Techniques

This far, the acquisition, processing, and properties of a single SAR image have been studied. However, if multiple acquisitions are available, additional information can be extracted from the data. Two advanced SAR techniques that will be discussed here are: SAR polarimetry (PolSAR) [96, 97], in which multiple polarisations are used to differentiate between different scattering mechanisms, and SAR interferometry (InSAR) [53], in which multiple SAR acquisitions made at slightly different incidence angles or at different occasions are used to study the position or the movement of the scattering phase centre.

PolSAR and InSAR form the basis for additional advanced SAR techniques: polarimetric SAR interferometry (PolInSAR) [59, 97], in which the principles of polarimetry and interferometry are combined; SAR tomography [98–100], in which a synthetic aperture is created in the vertical direction, and vertical scattering profiles

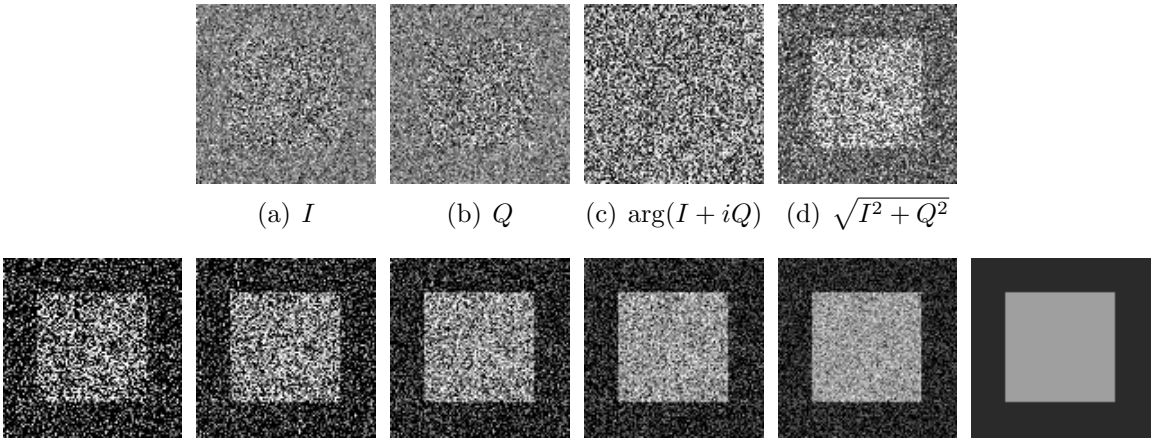

(a) I (b) Q (c) $\arg(I + iQ)$ (d) $\sqrt{I^2 + Q^2}$

(e) $\widehat{\sigma}_1$ (f) $\widehat{\sigma}_2$ (g) $\widehat{\sigma}_4$ (h) $\widehat{\sigma}_8$ (i) $\widehat{\sigma}_{16}$ (j) σ

Figure 2.8: Simulation showing the effect of number of looks on the intensity estimate. Figures (a)–(d) show the real and imaginary parts, phase, and amplitude of a one-look, complex Gaussian-distributed image. Figures (e)–(i) show the N-look intensity estimates in decibels, and Figure (j) shows the reference RCS, which is -3.0 dB for the central part and -6.7 dB for the outer part. Grayscale intervals are, from black to white: (a,b) $[-1, 1]$, (c) $[-\pi, \pi]$, (d) $[0, 1]$, and (e–j) $[-8\,\text{dB}, 0\,\text{dB}]$.

---

are estimated; polarimetric SAR tomography [47], in which the principles of polarimetry and tomography are combined; and SAR holography [101,102], in which circular, tomographic acquisitions are used to create three-dimensional images of the scene. These techniques will not be discussed here, but a good overview can be found in [6].

2.3.1 SAR Polarimetry

One of the basic properties of an EM wave is its polarisation, that is the direction of the electric field oscillations. In the far field from the scatterer, the oscillations of the EM wave are perpendicular to the direction of propagation, and if two perpendicular polarisations are used in a radar system both at transmission and reception, then the full scattering properties of the target at that particular frequency and incidence angle can be measured [96].

One of the most common polarisation bases used in SAR imaging is the horizontal-vertical basis. If the transmission is done with a horizontally polarised antenna (H), and the reception is done with a vertically polarised antenna (V), the polarisation mode is then called VH. Similarly, HH means that horizontal polarisation is used both at transmission and reception. If a system is capable of measuring all four combinations (HH, HV, VV, and VH) at the same time, together with their phase information, it is called fully polarimetric.

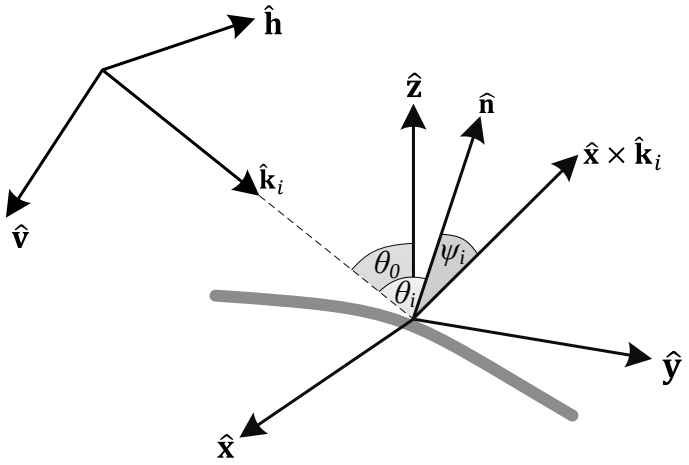

Figure 2.9: Basic scattering geometry. The incident wave is propagating in the direction of $\hat{\mathbf{k}}_i$, and oscillating in the plane defined by the horizontal and vertical vectors $\hat{\mathbf{h}}$ and $\hat{\mathbf{v}}$. The ground surface normal is $\hat{\mathbf{n}}$, θ_0 is the global incidence angle, θ_i is the local incidence angle, and ψ_i is the angle between the surface normal and image plane normal.

The electric field of an incident plane wave propagating in the direction of $\hat{\mathbf{k}}_i$, see Figure 2.9, can be expressed as a sum of two components, one in the horizontal direction and one in the vertical direction [96]:

$$\mathbf{E}^i = E^i_{\mathrm{H}}\hat{\mathbf{h}} + E^i_{\mathrm{V}}\hat{\mathbf{v}}, \tag{2.23}$$

where

$$\hat{\mathbf{h}} = \frac{\hat{\mathbf{z}} \times \hat{\mathbf{k}}_i}{|\hat{\mathbf{z}} \times \hat{\mathbf{k}}_i|} \tag{2.24}$$

is the horizontal unit vector, perpendicular both to the vertical axis and to the direction of propagation, and

$$\hat{\mathbf{v}} = \hat{\mathbf{h}} \times \hat{\mathbf{k}}_i \tag{2.25}$$

is the vertical unit vector, perpendicular both to the horizontal unit vector and the direction of propagation. Equivalently, the incident electric field can be written as a Jones vector [96]:

$$\mathbf{E}^i = \begin{bmatrix} E^i_{\mathrm{H}} \\ E^i_{\mathrm{V}} \end{bmatrix}. \tag{2.26}$$

Assuming plane waves, the Jones vector for the scattered field can be computed from the Jones vector for the incident field using [96]:

$$\mathbf{E}^s = \frac{e^{ikR}}{R}\,[S]\,\mathbf{E}^i, \tag{2.27}$$

where R is the distance between the target and the antenna, $k = 2\pi/\lambda$ is the wavenumber, and

$$[S] = \begin{bmatrix} S_{\mathrm{HH}} & S_{\mathrm{HV}} \\ S_{\mathrm{VH}} & S_{\mathrm{VV}} \end{bmatrix} \tag{2.28}$$

is the complex 2×2 scattering matrix. The scattering matrix fully describes scattering from the target at the current frequency and incidence angle.

The relation between the RCS and the scattering matrix elements can be obtained from the formal definition of the RCS [68]:

$$\sigma = \lim_{R\to\infty} 4\pi R^2 \frac{|\mathbf{E}^s|^2}{|\mathbf{E}^i|^2}, \tag{2.29}$$

which for polarisation PQ can be computed using (2.27):

$$\sigma_{\mathrm{PQ}} = 4\pi |S_{\mathrm{PQ}}|^2. \tag{2.30}$$

In remote sensing, most scatterers are not stable, fixed point targets, but they are distributed, dynamic targets stochastically changing in time and space. Such targets are best described using second order moments. The polarimetric covariance matrix contains all possible covariance combinations of the scattering matrix elements [96]. For a monostatic radar in a reciprocal medium, the cross-polarised terms of the scattering matrix are equal $S_{\mathrm{HV}} = S_{\mathrm{VH}}$ [103], and one of them is usually dropped or they are averaged to improve the SNR. To keep the total power invariant after dropping one element, the remaining cross-polarised term is usually scaled with $\sqrt{2}$ [96]. The polarimetric covariance matrix becomes:

$$[C] = \begin{bmatrix} \left\langle |S_{\mathrm{HH}}|^2 \right\rangle & \sqrt{2}\left\langle S_{\mathrm{HH}} S_{\mathrm{HV}}^* \right\rangle & \left\langle S_{\mathrm{HH}} S_{\mathrm{VV}}^* \right\rangle \\ \sqrt{2}\left\langle S_{\mathrm{HV}} S_{\mathrm{HH}}^* \right\rangle & 2\left\langle |S_{\mathrm{HV}}|^2 \right\rangle & \sqrt{2}\left\langle S_{\mathrm{HV}} S_{\mathrm{VV}}^* \right\rangle \\ \left\langle S_{\mathrm{VV}} S_{\mathrm{HH}}^* \right\rangle & \sqrt{2}\left\langle S_{\mathrm{VV}} S_{\mathrm{HV}}^* \right\rangle & \left\langle |S_{\mathrm{VV}}|^2 \right\rangle \end{bmatrix}, \tag{2.31}$$

where * is the complex conjugate operator.

Scattering coefficient sigma nought for polarisation mode PQ can be expressed in terms of the diagonal elements in (2.31) using (2.30) and (2.16):

$$\sigma^0_{\mathrm{PQ}} = \frac{\langle \sigma_{\mathrm{PQ}} \rangle}{A_{\mathrm{GR}}} = \frac{4\pi \left\langle |S_{\mathrm{PQ}}|^2 \right\rangle}{A_{\mathrm{GR}}} = \frac{4\pi \cos\psi_i \left\langle |S_{\mathrm{PQ}}|^2 \right\rangle}{A_{\mathrm{SR}}}, \tag{2.32}$$

where A_{SR} and A_{GR} are the areas of the resolution cells in slant range and ground range planes, respectively, and ψ_i is the angle between the image plane normal and ground surface normal, see Figure 2.9.

Scattering coefficient gamma nought can be computed from (2.32) using (2.18):

$$\gamma^0_{\mathrm{PQ}} = \frac{4\pi \cos\psi_i \left\langle |S_{\mathrm{PQ}}|^2 \right\rangle}{A_{\mathrm{SR}} \cos\theta_i}, \tag{2.33}$$

where θ_i is the local incidence angle, see Figure 2.9.

PolSAR data can be used to determine the dominant scattering mechanisms present within each pixel of the imaged scene using polarimetric decomposition theorems. There are several different types of decomposition theorems: coherent decompositions of the scattering matrix $[S]$ (e.g., the Pauli decomposition [96]), eigenvector and eigenvalue-based decompositions of the coherency matrix $[T]$ (e.g., the Cloude-Pottier or H/A/α decomposition [104]), and model-based decompositions of the covariance matrix $[C]$ or the coherency matrix $[T]$ (e.g., the Freeman-Durden three-component decomposition [105]). Polarimetric decomposition theorems are frequently used for land use classification, see [96].

2.3.2 SAR Interferometry

In SAR interferometry, the phase difference between two SAR images acquired over the same scene is used [53]. Two types of interferometry are common: across-track interferometry (XTI), in which the two images are acquired at slightly different incidence angles, and where the phase difference is used to estimate the scattering phase centre elevation, and along-track interferometry (ATI), in which the two images are acquired on different occasions, and where the phase difference is used to estimate the change in position of the scattering centre between the acquisitions. The most common application of the XTI technique is digital elevation model (DEM) creation, whereas the ATI technique can be used to estimate the radial velocity of, e.g., cars, ships, glaciers, ocean currents and waves, as well as ground surface deformations caused by earthquakes, volcanoes, landslides, etc.

The complex correlation coefficient (sometimes also called complex coherence) is the main interferometric observable. For two co-registered, complex SAR images S^1_{PQ} and S^2_{PQ}, it is defined as [53, 97]:

$$\widetilde{\gamma}_{=}\gamma \mathrm{e}^{i\Delta\phi} = \frac{\mathrm{E}\left[S^1_{\mathrm{PQ}} S^{2*}_{\mathrm{PQ}}\right]}{\sqrt{\mathrm{E}\left[\left|S^1_{\mathrm{PQ}}\right|^2\right]\mathrm{E}\left[\left|S^2_{\mathrm{PQ}}\right|^2\right]}}, \tag{2.34}$$

where $\gamma = |\widetilde{\gamma}|$ is called coherence and $\Delta\phi$ is the interferometric phase, i.e., the phase difference between the two images. Coherence is a real valued quantity between 0 and 1 and it is a measure of the degree of similarity between the two images. The phase difference is related to the difference in range to the scattering centre between the two images.

The complex correlation coefficient can be described as a product of four separate decorrelation effects [87, 106, 107]:

$$\tilde{\gamma} = \gamma_{\mathrm{SNR}}\tilde{\gamma}_{\mathrm{sys}}\tilde{\gamma}_{\mathrm{sp}}\tilde{\gamma}_{\mathrm{temp}}, \tag{2.35}$$

where the terms marked with the tilde sign may attain complex values.

SNR decorrelation γ_{SNR} is caused by thermal noise in the images and it can be determined from the SNR using [6, 106]:

$$\gamma_{\mathrm{SNR}} = \frac{1}{1 + SNR^{-1}}, \tag{2.36}$$

where it has been assumed that both images have the same SNR value.

System decorrelation $\tilde{\gamma}_{sys}$ is introduced by system imperfections, and it includes the effects of dynamic range, quantisation, misregistration, and ambiguities, as well as other errors introduced during SAR and InSAR processing [6,55]. Phase offsets may also be introduced in radar hardware and during processing. System decorrelation can be minimised with optimised electronics, signal processing, and calibration.

Spatial decorrelation $\tilde{\gamma}_{sp}$ is due to geometric differences between the two images. It can be re-stated as a product of three decorrelation terms [55]:

$$\tilde{\gamma}_{sp} = \tilde{\gamma}_{\mathrm{rg}}\tilde{\gamma}_{\mathrm{az}}\tilde{\gamma}_{\mathrm{vol}}, \tag{2.37}$$

where the first and second terms are decorrelation effects caused by differences in the sampled range and Doppler frequency spectra, respectively, and the last term is volume decorrelation. The first two decorrelation effects can be minimised through common-band filtering of both images [53,108,109]. The last term is a very important factor in XTI, as it carries information about the vertical distribution of the scatterers.

Temporal decorrelation $\tilde{\gamma}_{\mathrm{temp}}$ is due to the temporal changes in the imaged scene between the two acquisitions [87,106,110]. In the case of single-pass XTI the temporal decorrelation is most often negligible. In the case of repeat-pass XTI, this term is usually a nuisance that causes a loss of quality in the estimated DEM. In repeat-pass ATI, this term carries the information about the phase difference between the two acquisitions.

In the absence of decorrelation effects other than the volume decorrelation $\tilde{\gamma}_{\mathrm{vol}}$, the phase difference $\Delta\phi$ is determined by the difference in range to the scattering phase centre, called ΔR in Figure 2.10, but it is also affected by a 2π-phase ambiguity. The phase difference can be re-stated in terms of three phase components: the phase introduced by the difference in range to a reference height model (ΔR_0), the phase introduced by the elevation of the scattering phase centre above the reference height model (Δh), and a 2π-phase ambiguity [68,97]:

$$\Delta\phi = mk\Delta R + 2\pi n \approx k_z\left(\Delta R_0 \cos\theta_0 + \Delta h\right) + 2\pi n, \tag{2.38}$$

where m is equal to 2 for a monostatic system and 1 for a bistatic system, and where the vertical wavenumber is defined as [55,111]:

$$k_z = \frac{mkB_\perp}{R\sin\theta_0}, \tag{2.39}$$

where $B_\perp$ is the perpendicular baseline, θ_0 is the average incidence angle, and R is the average range to the scattering phase centre, as defined in Figure 2.10. The vertical wavenumber is the number of 2π-cycles corresponding to a vertical height shift of one metre.

In order to estimate Δh from $\Delta\phi$, it is necessary to remove the first and last phase components on the right hand side of (2.38). The removal of the phase caused by the differences in range to the reference height model, i.e., the first term in the

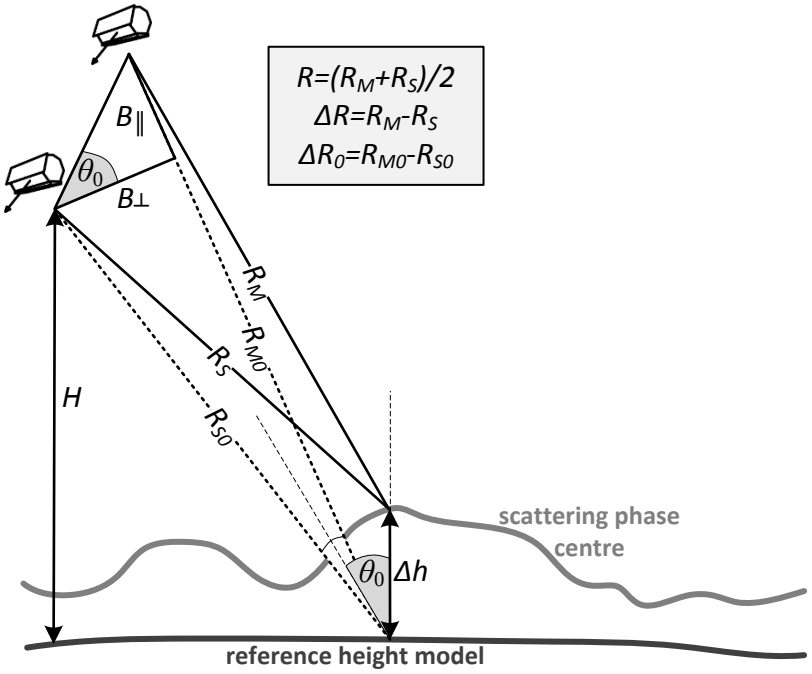

Figure 2.10: Simplified and exaggerated geometry for InSAR measurements. The reference height model may be flat earth, reference ellipsoid or geoid, or a DTM.

parenthesis in (2.38), is called flattening. Depending on application, different height models may be used: flat earth, geoid, ellipsoid, or a DTM. The removal of the 2π-phase ambiguity is called phase unwrapping. Phase unwrapping is often a non-trivial task and many different unwrapping algorithms have been developed [53].

Once both flattening and unwrapping have been performed, the elevation of the scattering centre above the reference height model can be estimated from the flattened and unwrapped phase difference $\Delta\phi'$ through a simple scaling:

$$\Delta h = \frac{1}{k_z}\Delta\phi'. \tag{2.40}$$

Instead of k_z, the more intuitive interferometric parameter height-of-ambiguity (HOA) is often used. It describes the vertical height shift equivalent to a 2π-phase shift and it is the maximal height difference that can be unambiguously resolved by an interferometric system. HOA is defined as:

$$\text{HOA} = \frac{2\pi}{k_z} = \frac{2\pi R \sin\theta_0}{mkB_\perp}. \tag{2.41}$$

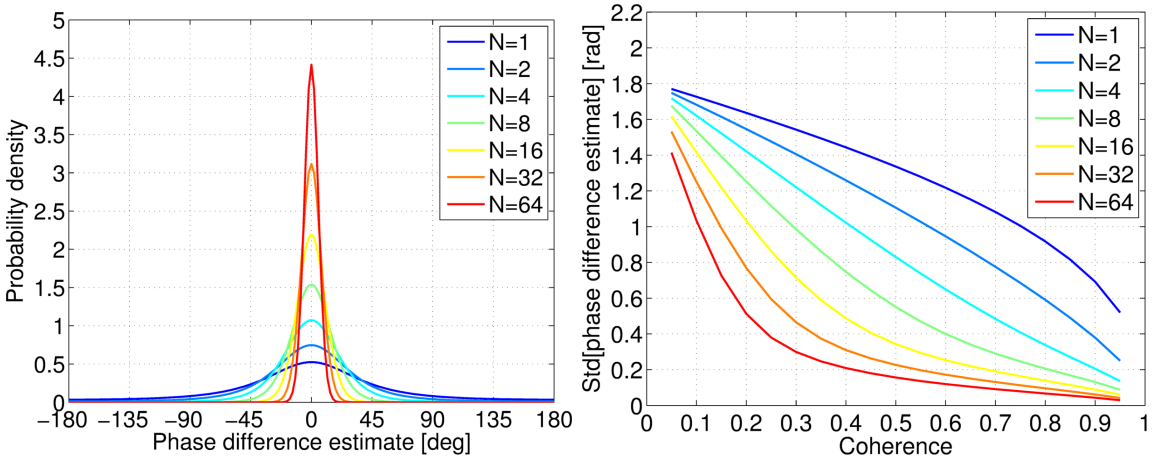

(a) Pdf ($\gamma = 0.7$) (b) Standard deviation

Figure 2.11: Statistics for the N-look phase difference estimate $\widehat{\Delta\phi}_N$.

2.3.2.1 InSAR Image Processing

The processing of InSAR imagery is a multi-step process. The first step consists of image co-registration [112, 113], in which one of the images is usually re-sampled to the range-azimuth grid of the second image. This includes both range and azimuth interpolation, as well as spectral filtering of the two images so that they cover the same 2D-frequency spectrum. This filtering procedure minimises the range and azimuth decorrelation effects [53, 108, 109]. The next step consists of interferogram creation, in which the first image is multiplied with the complex conjugate of the second image. Thereafter, flattening is conducted, in which a reference phase is removed (corresponding to flat earth, ellipsoid, geoid, or a DTM). Next, the flattened interferogram is multilooked, and the phase is computed and unwrapped. Finally, the unwrapped phase is scaled to height using a k_z or HOA map computed for the current acquisition geometry. A height calibration may be conducted here, e.g., using ground reference points. After this step, geocoding can be performed, to obtain the final DEM in a cartographic projection.

2.3.2.2 InSAR Image Statistics

In applications, the complex correlation coefficient is estimated using spatial averaging of N samples [53]:

$$\widetilde{\widehat{\gamma}}_N = \widehat{\gamma}_N e^{i\widehat{\Delta\phi}_N} = \frac{\frac{1}{N}\sum_i^N \left(S^1_{i,\mathrm{PQ}} S^{2*}_{i,\mathrm{PQ}}\right)}{\sqrt{\left(\frac{1}{N}\sum_i^N \left|S^1_{i,\mathrm{PQ}}\right|^2\right)\left(\frac{1}{N}\sum_i^N \left|S^2_{i,\mathrm{PQ}}\right|^2\right)}}, \tag{2.42}$$

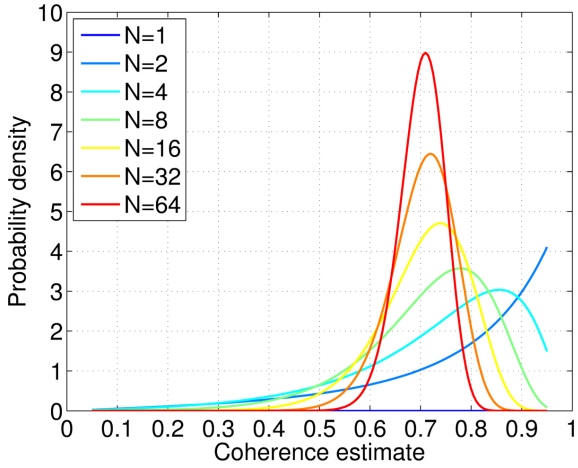

(a) Pdf ($\gamma = 0.7$)

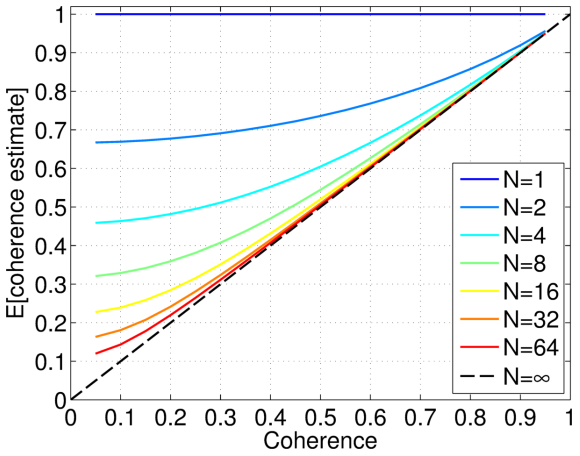

(b) Expectation value

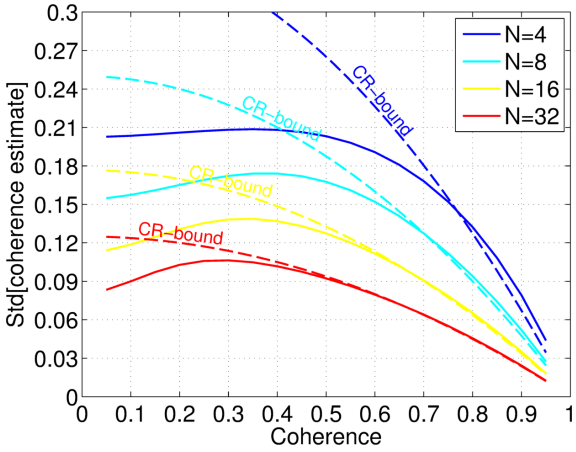

(c) Standard deviation

Figure 2.12: Statistics for the N-look coherence estimate $\widehat{\gamma}_N$. In (c), the dashed line shows the approximative standard deviation obtained with the Cramér-Rao (CR) bound.

---

where i is the sample index, and $\widehat{\gamma}_N$ and $\widehat{\Delta\phi}_N$ are N-look coherence and phase difference estimates.

The N-look phase difference estimate $\widehat{\Delta\phi}_N$ has the following pdf [53, 96]:

$$p(\widehat{\Delta\phi}_N|\Delta\phi, N, \gamma) = \begin{cases} \frac{\Gamma(N+\frac{1}{2})(1-\gamma^2)^N D}{2\sqrt{\pi}\Gamma(N)(1-D^2)^{N+\frac{1}{2}}} + \frac{(1-\gamma^2)^N}{2\pi} {}_2F_1(N, 1; \frac{1}{2}; D^2) & |\widehat{\Delta\phi}_N| < \pi \\ 0 & \text{otherwise} \end{cases}, \tag{2.43}$$

where $\Gamma(\bullet)$ is the gamma function, ${}_2F_1(\bullet)$ is the Gauss hypergeometric function, and

$$D = \gamma \cos(\widehat{\Delta\phi}_N - \Delta\phi). \tag{2.44}$$

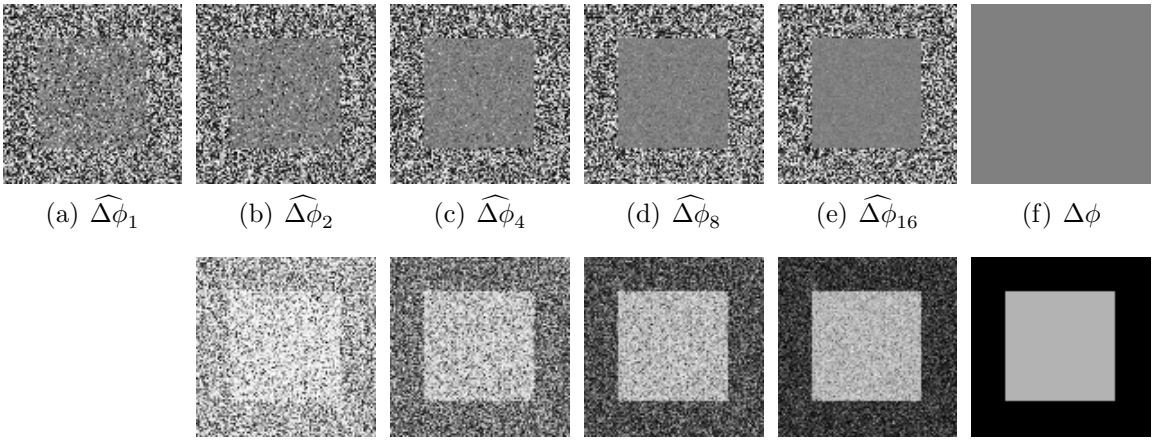

(a) $\widehat{\Delta\phi}_1$ (b) $\widehat{\Delta\phi}_2$ (c) $\widehat{\Delta\phi}_4$ (d) $\widehat{\Delta\phi}_8$ (e) $\widehat{\Delta\phi}_{16}$ (f) $\Delta\phi$

(g) $\widehat{\gamma}_1$ (h) $\widehat{\gamma}_2$ (i) $\widehat{\gamma}_4$ (j) $\widehat{\gamma}_8$ (k) $\widehat{\gamma}_{16}$ (l) γ

Figure 2.13: Simulation showing the effect of number of looks on the phase difference and coherence estimates. Figures (a)–(e) and (g)–(k) show the N-look phase difference and coherence estimates. Figure (f) shows the reference phase difference, which is zero for the entire image. Figure (l) shows the reference coherence, which is zero in the outer part and 0.7 in the central part. Grayscale intervals are, from black to white: (a–f) $[-\pi, \pi]$ and (g–l) $[0, 1]$. Note that the one-look coherence estimate is always equal to unity, which, for the chosen colour scale, results in a completely white image.

In Figure 2.11(a), the pdf for the N-look phase difference estimate $\widehat{\Delta\phi}_N$ is plotted for $\gamma = 0.7$ and $\Delta\phi = 0$. It can be observed that $\widehat{\Delta\phi}_N$ is an unbiased estimate of $\Delta\phi$, with standard deviation decreasing with increasing N. In Figure 2.11(b), the standard deviation is plotted against coherence for different numbers of looks N. The standard deviation decreases with increasing coherence and with increasing number of looks.

The N-look coherence estimate $\widehat{\gamma}_N$ has the following pdf [53]:

$$p(\widehat{\gamma}_N|\gamma, N) = \begin{cases} 2(N-1)(1-\gamma^2)^N \widehat{\gamma}_N (1-\widehat{\gamma}_N^2)^{N-2} {}_2F_1(N, N; 1; \widehat{\gamma}_N^2\gamma^2) & 0 \leq \widehat{\gamma}_N \leq 1 \\ 0 & \text{otherwise} \end{cases}. \tag{2.45}$$

In Figure 2.12(a), the pdf for the N-look coherence estimate $\widehat{\gamma}_N$ is plotted for $\gamma = 0.7$. It can be observed that for low N, coherence is overestimated and the standard deviation is high, but both the bias and standard deviation decrease with increasing N. In Figure 2.12(b), the expectation value for $\widehat{\gamma}_N$ is plotted against coherence for different numbers of looks N. The observed overestimation for low N is confirmed, and the bias is coherence-dependent. In Figure 2.12(c), the standard deviation of $\widehat{\gamma}_N$ is plotted against coherence for different N, together with the standard deviation given by the Cramér-Rao bound. As this is an approximation valid for

unbiased estimates, it can only be used when both N and γ are high [53]:

$$\mathrm{Var}[\widehat{\gamma}] = \frac{(1-\gamma^2)^2}{2N}. \tag{2.46}$$

Simulation results for the N-look phase difference and coherence estimates are shown in Figure 2.13. In Figures 2.13(a)–2.13(e), the N-look phase difference estimates are shown. It can be observed that in the central region, the variance of the phase difference decreases with an increasing number of looks. However, for the outer part of the images, the phase difference is equally noisy for any number of looks. This is due to the fact that coherence in that region is zero. The reference phase difference is zero for the entire image, see Figure 2.13(f).

In Figure 2.13(g), the one-look coherence estimate is shown, and it is equal to unity for the entire image. For an increasing number of looks, the coherence overestimation decreases, see Figures 2.13(h)–2.13(k). The reference coherence is shown in Figure 2.13(l). In the central part, the coherence is 0.7, whereas in the outer part, it is zero.

2.4 Past, Present, and Future SAR Systems

As mentioned earlier, more than 15 civilian, spaceborne SAR systems are currently operational and around 10 are planned to be launched within the next five years [6,78]. Due to the major advantages of polarimetry and interferometry, most modern SAR systems are designed to be able to provide PolSAR and/or InSAR data.

Airborne systems are used to acquire SAR data in cases when satellite SAR data are unavailable or insufficient, e.g., in campaigns associated with preparatory studies for new satellite systems. Airborne SAR systems have the advantage of being easy to deploy and affordable on lower scales.

2.4.1 PolSAR Systems

Presently, two civilian, fully polarimetric SAR systems are operational: the C-band RADARSAT-2 system from the Canadian Space Agency (CSA) [114] and the L-band ALOS-2 PALSAR-2 system from the Japan Aerospace Exploration Agency (JAXA) [115]. Moreover, the X-band TerraSAR-X and TanDEM-X systems from the German Aerospace Center (DLR) are able to provide fully-polarimetric data in the experimental mode [55], whereas the C-band RISAT-1 system from the Indian Space Research Organisation (ISRO) is able to provide hybrid-polarimetric SAR data (circular polarisation on transmission, linear polarisations on reception) [116].

In May 2013, ESA selected BIOMASS for the 7th Earth Explorer mission [51]. BIOMASS will feature a fully-polarimetric SAR sensor operating at the centre frequency of 435 MHz with a bandwidth of 6 MHz, giving a nominal slant range resolution of 25 m [3]. It will be the first P-band SAR sensor in space, with the main goal

to provide global biomass, forest height, and deforestation maps. Due to the low frequency, repeat-pass interferometry and tomography over forests will be feasible with BIOMASS. The launch of BIOMASS is currently scheduled for 2020.

Papers A and B appended to this thesis summarise the results obtained within the BIOMASS feasibility study. In these papers, P-band SAR data acquired with the airborne Experimental-SAR (E-SAR) system [117–119] from the DLR are used, acquired within the BioSAR 2007 and 2008 campaigns [41,120]. The centre frequency of this system was 360 MHz, which is lower than for BIOMASS, with a bandwidth of up to 100 MHz. The E-SAR system was decommissioned in 2008 and replaced by the F-SAR system [121].

2.4.2 InSAR Systems and Satellite Constellations

All modern SAR systems are coherent and repeat-pass interferometry can, in theory, be conducted using any satellite system, but the temporal decorrelation often limits the applications. Temporal decorrelation can be decreased either by using the lower frequency bands (as in the case of the P-band SAR system BIOMASS), or by using multiple sensors. Moreover, the use of multiple sensors in a constellation significantly increases both the coverage and acquisition frequency, which is beneficial for large-scale monitoring and reconnaissance purposes.

Two current SAR constellation missions capable of providing global imagery at daily rates are: the dual-purpose (civil and military) COSMO-SkyMed system of four X-band satellites from the Italian Space Agency (ASI) [122], and the military SAR-Lupe system of five X-band satellites from the DLR [123]. The civilian Sentinel-1a satellite, launched by ESA in 2014, is the first of two C-band SAR systems, which together will be able to provide SAR imagery of the entire Europe every third day [124]. Moreover, the S-band system HJ-1C, launched in 2012, is the first of four SAR satellites planned for a constellation mission from the Chinese Academy of Science and Technology (CAST) [125].

The X-band PAZ system, funded by the Spanish Center for Development of Industrial Technology (CDTI) and scheduled to be launched in 2014, is planned to operate in constellation with the almost identical satellites TerraSAR-X and TanDEM-X [126, 127]. The SAOCOM-1A/B mission from the Argentine National Commission for Space Activities (CONAE) will consist of two fully-polarimetric, L-band SAR satellites [128], planned to be launched in 2015 and 2016, respectively. The RADARSAT Constellation Mission of three C-band satellites from the CSA is planned to be launched in 2018, with the main task to provide daily imagery of the Canadian lands and oceans [129].

Single-pass interferometric SAR systems have the advantage of low temporal decorrelation, but they require multiple SAR sensors in a close formation. Currently, spaceborne single-pass InSAR data can be acquired only with the TanDEM-X system, consisting of the previously mentioned satellites TerraSAR-X and TanDEM-X in a tight helix formation [55]. The main goal of the TanDEM-X mission is to acquire

the first, fully global DEM with a spatial resolution of $12\,\mathrm{m} \times 12\,\mathrm{m}$ and an absolute vertical accuracy better than $10\,\mathrm{m}$ [130], which will replace the older DEM acquired within the Shuttle Radar Topography Mission (SRTM) from the space shuttle Endeavour in February 2000. Papers C, D, and E appended to this thesis are focussed on forest parameter estimation from TanDEM-X data.

The proposed ESA SAOCOM-CS mission will feature a passive SAR sensor in a formation flight with the SAOCOM-1B satellite [64]. Also, a TanDEM-L mission has been proposed, consisting of two L-band satellites in a tight tandem formation and providing fully-polarimetric, high-resolution data in a wide-swath mode [65].

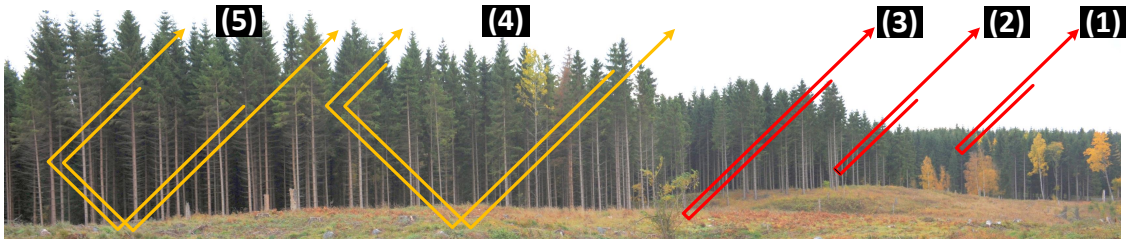

Figure 3.1: Some of the most significant scattering mechanisms in forest: direct backscatter from (1) tree canopies, (2) tree trunks, and (3) ground surface, and double-bounce interactions between (4) ground surface and tree canopies, as well as between (5) ground surface and tree trunks.

Chapter 3

Microwave Scattering from Forests

When studying forests with SAR imagery, it is important to be able to separate the influence of system parameters from the influence of geo- and biophysical forest parameters. Scattering models are important tools which can improve the understanding of the electromagnetic interactions.

Accurate modelling of electromagnetic scattering from forests can be achieved by means of computational electromagnetics, in which Maxwell's equations are solved numerically for a discretised forest model. However, the computational costs of this approach can be enormous, especially if multiple evaluations are required, e.g., in case when the influence of a system parameter on the scattering coefficient needs to be examined.

In many cases, the usefulness of a simplified model is of higher priority than extreme accuracy, e.g., when the model is to be used to explain the cause of a particular effect observed in the experimental data. In such cases, simplifications can be made by replacing complicated forest elements with simple objects, for which fast analytical solutions are available, and by reducing the number of modelled interactions.

The accuracy of such simplified models depends primarily on two factors: if all the most important scattering mechanisms are modelled, and how well each scattering mechanism is modelled.

3.1 Basic Scattering Mechanisms

In some of the most common models [132–136], forest is composed of three types of elements: ground surface, tree trunks, and tree canopies. Each of these elements contributes both on its own and in combination with the other elements to the total backscattered field. The most significant, low-order scattering mechanisms shown in Figure 3.1 are:

(1) direct backscatter from tree canopies,

(2) direct backscatter from tree trunks,

(3) direct backscatter from the ground surface,

(4) double-bounce interactions between the ground surface and tree canopies,

(5) double-bounce interactions between the ground surface and tree trunks.

Higher-order mechanisms and near-field interactions can often be neglected. Due to reciprocity, the two double-bounce interactions between the same elements, but in reversed order (e.g., ground-trunk and trunk-ground), are equivalent and they add up in phase, acting as one single scattering mechanism [137]. In the following, oblique incidence angles and vertical or near-vertical tree trunks will be assumed.

3.1.1 Direct Backscatter

Direct backscatter is primarily caused by reflections from surfaces facing the radar antenna. Therefore, most of the direct backscatter occurs in the canopy, from rough surfaces, and from occasional slopes facing the radar antenna.

Canopies consist of more or less randomly oriented branches of different sizes, as well as needles or leaves. Canopy backscatter is generally stronger at high frequencies, when the scatterers are comparable to, or larger than the wavelength [95]. Consequently, penetration through the canopy is expected to decrease with increasing frequency. If the scatterers in the canopy have a preferred orientation, the backscattered field will show polarisation dependence.

Surface roughness is characterised in relation to the wavelength, and a surface which is rough at high frequencies may be smooth at low frequencies [91, 138]. At oblique incidence, backscattering from a randomly rough surface is stronger than from a smooth surface. Many realistic surfaces, such as forest soil and bark, may be treated as slightly rough surfaces when the wavelength is much longer than the surface irregularities (e.g., at P-band) and very rough surfaces when the surface irregularities

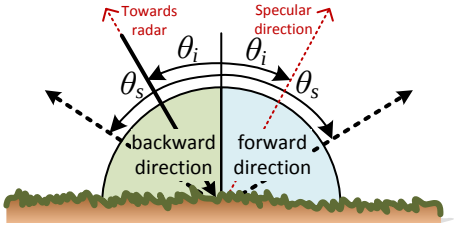

(a) Scattering geometry

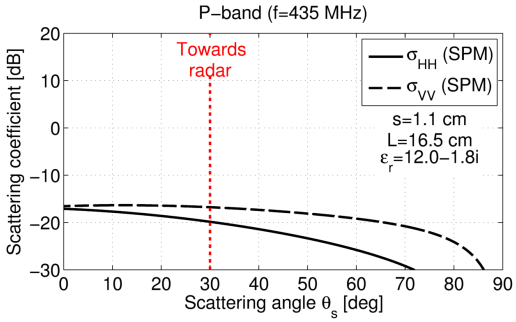

(b) Backward direction (slightly rough surface at P-band)

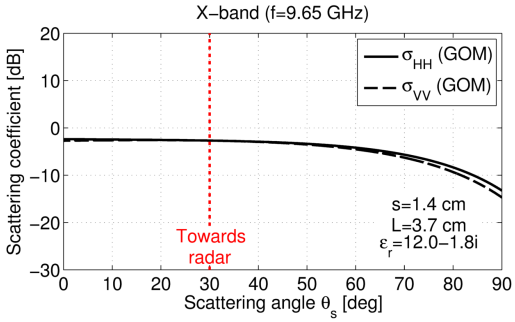

(c) Backward direction (very rough surface at X-band)

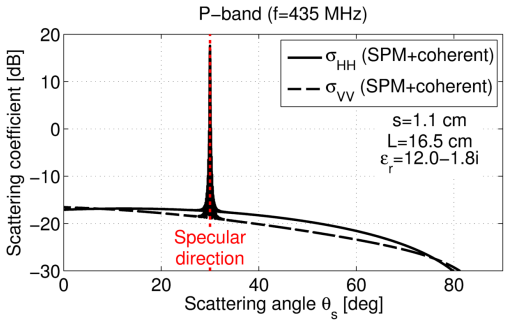

(d) Forward direction (slightly rough surface at P-band)

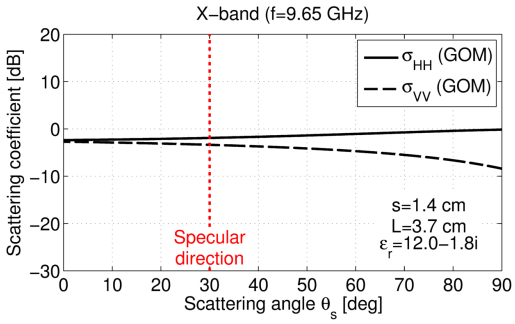

(e) Forward direction (very rough surface at X-band)

Figure 3.2: Scattering from a slightly rough surface (P-band) and a very rough surface (X-band), corresponding to low- and high-frequency regimes, respectively. In all cases, the incidence angle θ_i is 30° and only scattering in the incidence plane is studied. Non-coherent rough surface scattering has been modelled using the geometrical optics model (GOM) in the high-frequency regime and the small perturbation model (SPM) in the low-frequency regime, using the expressions found in [103]. Coherent scattering is only significant for the slightly rough surface in the forward direction, where it has been modelled using the expression presented in [91] and assuming a circular surface with a radius of 100 m. Parameters s and L are the standard deviation of the vertical variations and the correlation length of the rough surface, and together with the relative dielectric constant ε_r, their values have been chosen based on [131].

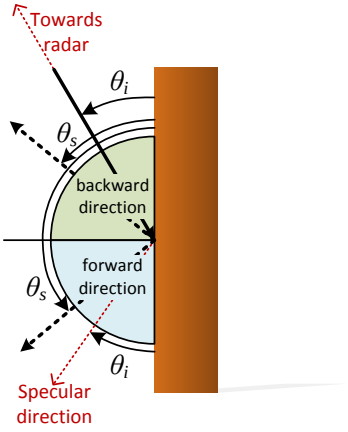

(a) Scattering geometry

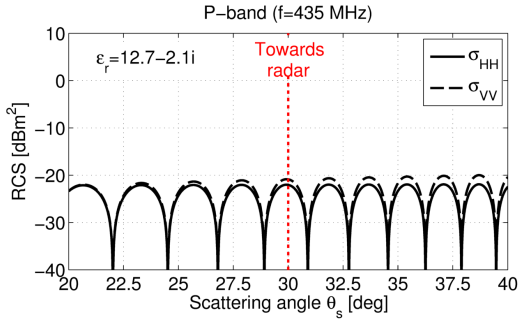

(b) Backward direction (P-band)

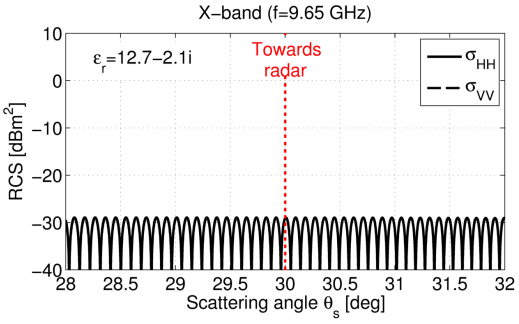

(c) Backward direction (X-band)

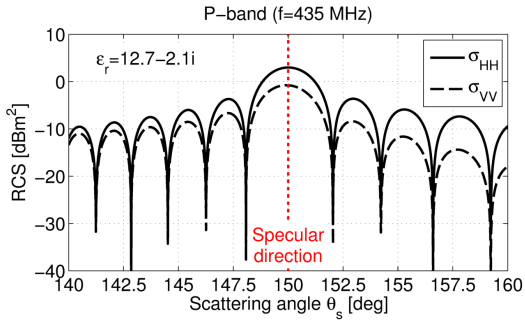

(d) Forward direction (P-band)

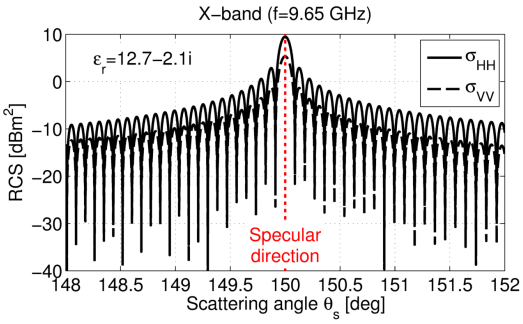

(e) Forward direction (X-band)

Figure 3.3: Scattering from a smooth vertical cylinder modelled using the infinite cylinder approximation [103]. In all cases, the incidence angle θ_i is 30° and only scattering in the incidence plane is studied. The cylinder has a length of 20 m, radius of 13 cm, and the relative dielectric constant ε_r chosen according to [17]. Note the significant difference in the scales of the x-axes.

are comparable to, or larger than the wavelength (e.g., at X-band). Therefore, direct backscatter from such surfaces is expected to be stronger at high frequencies.

In Figure 3.2(b) and Figure 3.2(c), rough surface scattering in the backward direction is modelled at P- and X-bands using the small perturbation model (SPM) and the geometrical optics model (GOM), respectively. The SPM is a low-frequency approximation, valid when surface roughness is small in comparison to the wavelength, whereas the GOM is a high-frequency approximation, valid for very rough surfaces [103]. At P-band, with a centre frequency of 435 MHz and a wavelength of 69 cm, the chosen roughness parameters (standard deviation of vertical variations equal to 1.1 cm and the surface correlation length equal to 16.5 cm) correspond to a slightly rough surface. Backscattering is thus very weak, see Figure 3.2(b). At X-band, with a centre frequency of 9.65 GHz and a wavelength of 3.1 cm, the chosen roughness parameters (standard deviation equal to 1.4 cm and correlation length equal to 3.7 cm) correspond to a very rough surface. Backscattering is therefore much stronger, see Figure 3.2(c). Note that roughness parameters have been chosen according to [131], for optimal validity of the asymptotic models. The surfaces are therefore slightly different for the two studied cases (P- and X-band).

In Figure 3.3(b) and Figure 3.3(c), scattering in the backward direction from a smooth, vertical cylinder is modelled at both P- and X-bands using the infinite cylinder approximation [103]. As it can be observed, the backscattering coefficient is low in both cases. Note, however, that in more realistic scenarios, trunks are not smooth vertical cylinders, but they attain a rougher and possibly also curved form. Therefore, backscattering from a tree trunk will be stronger in reality.

3.1.2 Double-Bounce Interactions

Double-bounce interactions require a strong specular reflection from the ground as well as from the trunks and/or canopies. A smooth surface will generally have a stronger specular component than a rough surface [91, 138], and for many natural rough surfaces, double-bounce interactions will be more common for the lower frequencies. The strength of the double-bounce interactions between the ground surface and vertical trunks will be affected by the ground slope and by the relative length of the trunks. At lower frequencies, the trunks will be shorter relative the wavelength, resulting in a wider forward scattering lobe [139], and the double-bounce interaction will be less sensitive to ground slope. For a ground surface tilted in the azimuth direction, double-bounce interaction will be present also in the cross-polarised channel [17].

In Figure 3.2(d) and Figure 3.2(e), rough surface scattering in the forward direction is modelled at P- and X-bands using the SPM (with a coherent term) and the GOM, respectively, at an incidence angle of 30°. For P-band and the slightly rough surface, forward scattering is weak in all cases except when the scattering angle is around 30°, i.e., in the specular direction, when the coherent term becomes significant. The width of the coherent scattering lobe depends on the size of the surface; a larger

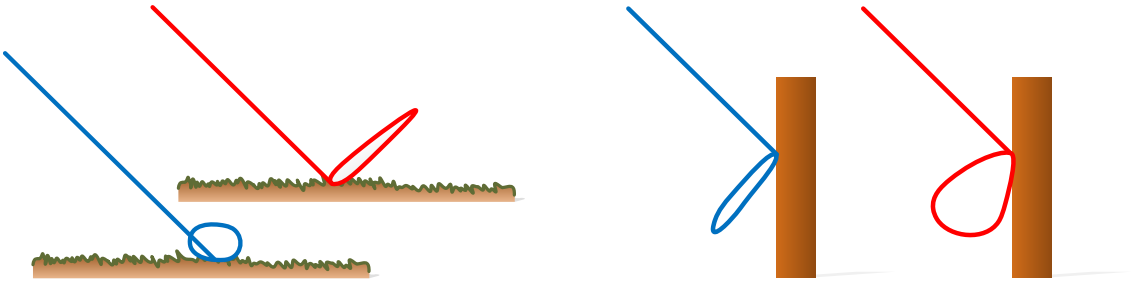

(a) Rough surface (b) Smooth cylinder

Figure 3.4: Simplified visualisations of rough surface scattering and reflection from a smooth cylinder in **high**- and **low**-frequency regimes (in blue and red, respectively).

surface results in a narrower lobe and a stronger specular reflection. For X-band and the very rough surface, forward scattering in non-specular directions is stronger than for a slightly rough surface, whereas the coherent component is negligible.

In Figure 3.3(d) and Figure 3.3(e), scattering in the forward direction from a smooth, vertical cylinder is modelled at both P- and X-bands using the infinite cylinder approximation. The forward scattering lobe is wider for P-band, although the scattering coefficient in the specular direction is lower.

Double-bounce interactions between the ground surface and tree canopies are often weak, due to the high penetration capabilities at low frequencies, when the specular reflection from the ground is the strongest.

3.1.3 Dominant Mechanisms at P- and X-bands

At P-band, direct backscatter from larger branches in the canopies and ground slopes facing the antenna, as well as the double-bounce interactions between ground and trunks are expected to be the strongest contributions, the latter due to the strong specular reflection from relatively smooth surfaces and wide forward scattering lobe from the trunks, see Figure 3.4. The strength of these contributions is related to the volume of the trunk, but it also depends on the dielectric properties of the elements, roughness of both ground and trunk surfaces, and the ground topography. Several models of dielectric cylinders over ground have been developed for lower frequencies [17, 140–143].

At X-band, direct backscatter is expected to be the main contribution, due to the random orientation of the canopy scatterers, and the relatively rough trunk and ground surfaces, see Figure 3.4. Direct backscatter from the rough trunk and ground surfaces is expected to be strong only in the case of sparse canopies, i.e., when penetration through canopy gaps is significant. In general, low sensitivity to biomass is expected for the backscattered signal at X-band due to the strong dependence on

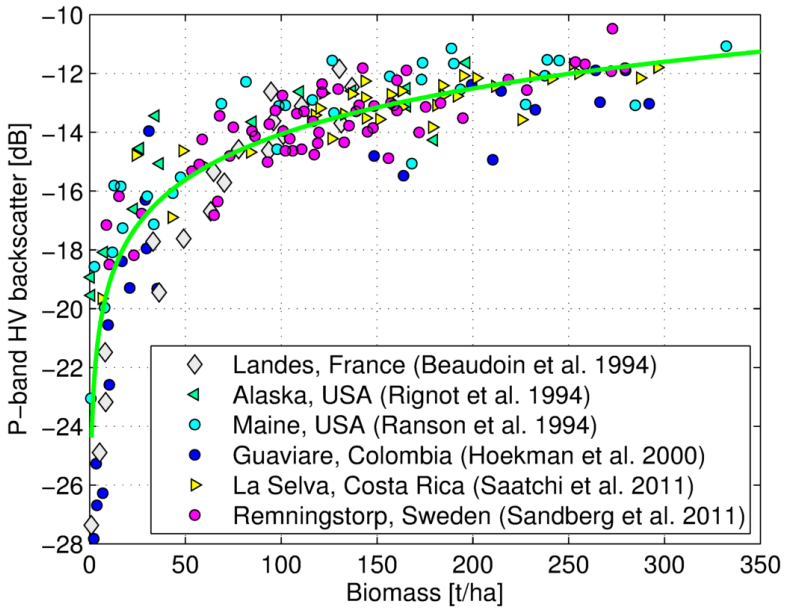

Figure 3.5: A power law function relating backscatter coefficient gamma nought to biomass is here plotted with the green, solid line, together with backscatter data from six airborne SAR campaigns. The referenced studies can be found in [26, 28, 32, 36, 37, 144]. The figure has been adapted from [38]. Note that the original data from La Selva and Remningstorp have been corrected with +5 dB and -3 dB, respectively, to compensate for the observed offset from the other four data sets.

surface roughness and the weak dependence on the trunk volume.

Polarisation and incidence angle dependence is expected to be stronger at P-band, due to the stronger contribution of the ground surface and tree trunks, which are often less randomly oriented than the canopy scatterers.

3.2 Models for Forest Scattering

Scattering models serve as a link between theory and empirical observations. Therefore, the development of models can be approached from both ends, and two general model types can be distinguished: empirical and theoretical.

3.2.1 Empirical Models

Empirical models are derived from observations in the experimental data. Using regression analysis, functions can be fitted to the data and used to explain the observed behaviour. As both the experimental data and model selection strategies may vary

(a) IWCM (b) RVoG

Figure 3.6: Two vertical backscatter profiles used by the IWCM and RVoG models.

significantly between different studies, the number of empirical models available in the literature is very large.

The power law is one of the more popular models, which can be used to explain many phenomena observed in nature [145,146]. In SAR remote sensing of forests, this function is often used to describe the relation between the backscattering coefficient and biomass, especially for HV-polarised, P-band data. In [38], the following power law function has been fitted to HV-polarised data from six airborne P-band SAR campaigns conducted in different biomes on three different continents:

$$\gamma^0_{\mathrm{HV}} = a\mathcal{B}^b, \tag{3.1}$$

where $\mathcal{B}$ is biomass in tons per hectare and a and b are model parameters. After correction of an observed offset in γ^0_{HV} in two of the six data sets, the same parameters a and b can be used for all six data sets, see Figure 3.5.

3.2.2 Theoretical Models

Theoretical models are created using simple objects for which approximative analytical solutions exist (cylinders, rough surfaces, discs, needles, dipoles, etc.). There are two main types of theoretical models: coherent and non-coherent.

Coherent models are based on wave propagation and Maxwell's equations, and the contributions from the different scattering mechanisms are added in phase. Common coherent models include models based on the cylinder-over-ground approximation, which are primarily used to model the trunk-ground interactions at lower frequencies [17, 140, 141, 143, 147–149], as well as more complex models with more elements and higher-order interactions [136, 150–152].

Non-coherent models are based on energy propagation and radiative transfer equations. Therefore, no correlation between the fields scattered by the different elements is assumed, and the contributions of the different scattering mechanisms are added in terms of power. The analytical treatment of these models is generally simpler. Many non-coherent models have been developed in the past [132, 133, 153–157].

3.2.2.1 Interferometric Models

In across-track interferometry, modelling of volume decorrelation can be done from the vertical backscattering profile $\sigma_{\mathrm{v}}(z)$ using [106, 110]:

$$\tilde{\gamma}_{\mathrm{vol}} = \frac{\int_{-\infty}^{\infty} \sigma_{\mathrm{v}}(z) e^{ik_z z} \mathrm{d}z}{\int_{-\infty}^{\infty} \sigma_{\mathrm{v}}(z) \mathrm{d}z}. \tag{3.2}$$

Two simple models have been frequently used since the late 90's for forest parameter estimation from InSAR data. In both models, vegetation canopy is modelled as a water cloud, as proposed in [94], and ground is modelled as an impenetrable surface. As the scattering centres of the double-bounce interactions are located at the ground level, the double-bounce interactions do not have to be modelled separately.

In the interferometric water cloud model (IWCM) [57, 58], vegetation is modelled as a homogeneous volume of randomly oriented scatterers located above a ground plane and covering a certain fraction of the total area, called the area-fill factor, see Figure 3.6(a). It has been shown in [94], that the effective attenuation of the random volume can be described by an exponential backscatter profile function. The vertical backscattering profile $\sigma_{\mathrm{v}}(z)$ can then be formulated as:

$$\begin{aligned} \sigma_{\mathrm{v}}(z) &= \eta \left[\sigma^0_{\mathrm{veg}} \alpha e^{-\alpha(z_0+h-z)} \Theta(z_0+h-z)\Theta(z-z_0) \right. \\ &\quad \left. + \sigma^0_{\mathrm{gr}} \delta(z-z_0) e^{-\alpha h} \right] + (1-\eta)\delta(z-z_0)\sigma^0_{\mathrm{gr}}, \end{aligned} \tag{3.3}$$

where η is the area-fill factor, σ^0_{gr} and σ^0_{veg} are the effective ground and vegetation backscattering coefficients, α is the extinction coefficient, z_0 is the ground elevation, h is the volume height, $\delta(\bullet)$ is the Dirac delta function, and $\Theta(\bullet)$ is the Heaviside step function. By inserting (3.3) into (3.2), the total volume decorrelation can be obtained.

The IWCM was originally developed for stem volume estimation from repeat-pass interferometric, C-band ERS-1/2 data [57, 58], where it was fitted to coherence and backscatter data, which were found stable in winter conditions in various forests [158–161] (the phase information was not used due to high temporal decorrelation [162]). Therefore, the full formulation of the IWCM also includes two temporal decorrelation terms (one for the ground and one for the volume parts) and an allometric relation between height and stem volume. Additionally, an empirical model relating stem volume to backscattering coefficient and first published in [163] is also included, to make backscatter modelling agree with the empirical observations. IWCM fitting is usually done collectively for all data points using training data, effectively making the model parameters into site-dependent constants.

In the random volume over ground (RVoG) model [59–61, 164], the profile used in the IWCM is simplified by neglecting the canopy gaps, see Figure 3.6(b):

$$\sigma_{\mathrm{v}}(z) = \sigma^0_{\mathrm{veg}} \alpha e^{-\alpha(z_0+h-z)} \Theta(z_0+h-z)\Theta(z-z_0) + \sigma^0_{\mathrm{gr}} \delta(z-z_0) e^{-\alpha h}. \tag{3.4}$$

The traditional use of the RVoG model includes forest height and ground elevation estimation from PolInSAR data [44,45,59–61,164,165]. Model fitting is generally done

on a pixel-by-pixel basis, by balancing the number of observables with the number of parameters. In recent years, the RVoG model was further developed, and the estimation of vertical scattering profiles [99, 166] as well as temporal decorrelation [167] from PolInSAR data were introduced.

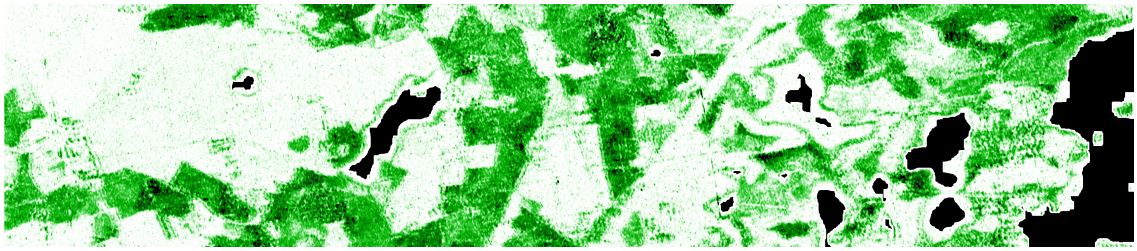

Chapter 4

Summary of the Appended Papers

This chapter begins with a short presentation of the reference data used in the appended papers. Thereafter, the appended papers are presented, first the two P-band papers and then the three X-band papers.

4.1 Experimental Data

Two test sites located in Sweden are used in the appended papers: Remningstorp and Krycklan, see Figure 4.1. The distance between these test sites is approximately 720 km.

Remningstorp (58° 28' N, 13° 38' E) is a hemi-boreal forest site situated in southern Sweden, approximately 150 km north-east of Gothenburg (Göteborg). The test site is fairly flat, with ground slopes at stand level lower than 5° (computed from a 50 m × 50 m DTM). Remningstorp covers approximately 1200 ha of productive forest land, and the forest consists primarily of Norway spruce (*Picea abies* (L.) Karst.), Scots pine (*Pinus sylvestris* L.), and birch (*Betula* spp.). Remningstorp has been used in the two ESA-funded campaigns BioSAR 2007 and 2010 [41, 42], conducted in support to the BIOMASS feasibility study [3].

Krycklan (64° 14' N, 19° 46' E) is a boreal forest site located in northern Sweden, approximately 50 km north-west of Umeå. Compared to Remningstorp, Krycklan has a more strongly undulating topography, with ground slopes on stand level reaching

Figure 4.1: The two test sites used in the appended papers, Remningstorp and Krycklan, separated by 720 km.

19° (computed from a 50 m × 50 m DTM). Krycklan covers approximately 6700 ha of forested land, which is dominated by Norway spruce and Scots pine. Krycklan has been used in the ESA-funded campaign BioSAR 2008 [120], conducted in support to the BIOMASS feasibility study [3].

For each test site, several sets with reference data have been provided by the Swedish University of Agricultural Sciences (SLU). The data can be divided in three categories: plot-level data, stand-level data, and maps.

Stands are relatively homogenous forest regions with similar species composition, biophysical characteristics (e.g., tree height and tree number density), and management procedures. They can vary in size and shape, and they are the main unit used for forest mapping and management [11]. Plots are usually smaller stand subsets of regular shape, which are used as within-stand samples. Often, they are distributed in a systematic grid covering the test site or a stand.

Although the exact methodologies used during field inventories may vary between the individual reference data sets, the general approach is similar. Commonly, the relevant and easily accessible parameters such as stem diameter at breast height (dbh) and tree species are sampled for all trees confined within plot borders and fulfilling a minimum dbh criterium (dbh larger than 4 cm in Krycklan; dbh larger than 5 cm in Remningstorp). For a subset of these trees, the more time-consuming measurements of, e.g., tree height and age, are made. Plot- and stand-level estimates are then computed from the sampled tree parameters, and biomass is estimated using allometric equations, for example the Marklund or Petersson formulas [168, 169]. In recent years, the forest management system Heureka [170] has been frequently used for forest parameter estimation from *in situ* data.

Maps of forest parameters are usually derived from airborne lidar scanning (ALS) data. In ALS, laser pulses transmitted downwards from an aircraft or a helicopter are used to sample canopy height at high vertical and horizontal resolutions. From the sampled pulses, different lidar-based estimates of forest parameters are obtained, and biomass maps are created using regression analysis and plot-level reference data.

The accuracy of plot-, stand-, and map-level biomass estimates depends on many factors: measurement error, the uncertainty in the allometric models, natural variation in the data, sampling density, etc. Moreover, correlation between error sources is not uncommon and need to be considered. When evaluating the performance of SAR-based biomass estimation algorithms, it is important to consider the uncertainties in the reference data.

4.2 Paper A

In this paper, a P-band polarimetric-interferometric forward model (FM) is developed and used to model SAR imagery acquired with the airborne E-SAR system over Remningstorp. The FM is used within the BIOMASS end-to-end simulator (BEES), used by ESA to assess the error budget of the proposed (now selected) mission BIOMASS [3, 52].

In accordance with the requirements from ESA, the FM predicts the extended covariance matrix scaled to sigma nought on the diagonal from a small number of geo- and biophysical forest and system parameters. The influence of scene moisture and ground slopes is not modelled.

Four model scenarios have been developed for BEES, featuring two different backscatter profiles (exponential and truncated Gaussian) for two different biomes (tropical and boreal). However, only the boreal scenario with the exponential profile is studied in Paper A. For a full description of the model and the different scenarios, consult [171].

The extended covariance matrix is a matrix with all covariance combinations of the unique elements of two scattering matrices, one for each interferometric acquisition. Assuming a monostatic system, reciprocal and reflection symmetric medium, and identical polarimetric response at both ends of the baseline, the extended co-

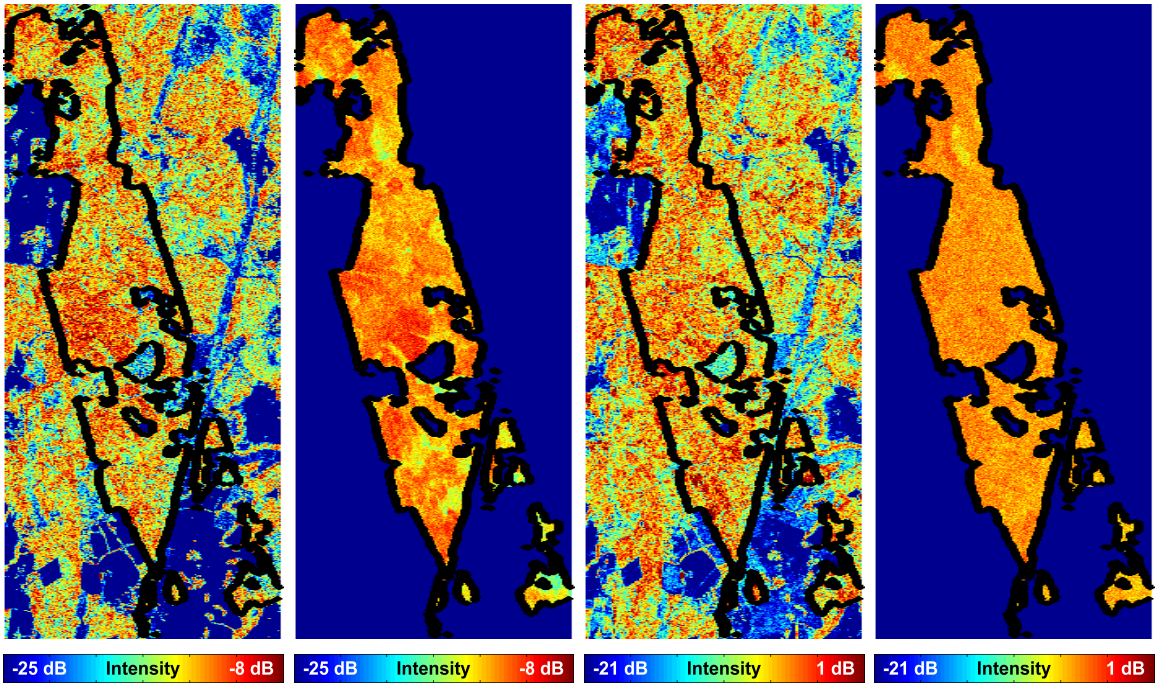

(a) Reference (HV) (b) Modelled (HV) (c) Reference (VV) (d) Modelled (VV)

Figure 4.2: In Paper A, the extended covariance matrix is modelled for P-band from a few forest and system parameters. Here, backscatter coefficients sigma nought modelled from biomass and incidence angle maps are compared to the reference data acquired with the airborne E-SAR sensor. The test site is Remningstorp and the black contours mark the area covered by the biomass map. Outside, biomass has been set to zero.

---

variance matrix is a 6×6 matrix, and it can be re-stated in terms of three basic quantities: three real-valued backscatter coefficients sigma nought (one for each polarisation), three complex-valued interferometric correlation coefficients (one for each polarisation), and one complex-valued polarimetric correlation coefficient (between the two co-polarised channels).

Backscatter coefficients are for all polarisations modelled in decibels using a linear function of biomass, based on (3.1), and an additive, zero-mean Gaussian noise term. Model parameters and noise variance are estimated from the training data:

$$[\gamma^0_{\mathrm{HH}}]_{\mathrm{dB}} = -20.1 + 8.1 \log_{10} \mathcal{B} + \mathrm{N}(0, 1.3^2), \tag{4.1}$$

$$[\gamma^0_{\mathrm{HV}}]_{\mathrm{dB}} = -20.7 + 4.2 \log_{10} \mathcal{B} + \mathrm{N}(0, 0.7^2), \tag{4.2}$$

$$[\gamma^0_{\mathrm{VV}}]_{\mathrm{dB}} = -6.7 + 0.6 \log_{10} \mathcal{B} + \mathrm{N}(0, 1.2^2), \tag{4.3}$$

where $\mathcal{B}$ is the biomass in tons per hectare. As it can be observed, the highest

sensitivity to biomass is obtained for the HH-channel, but with a larger variance. For the HV-channel, the sensitivity is still high, and the variance is lower. For the VV-channel, the sensitivity to biomass is very low.

Interferometric correlation coefficients are for all polarisations modelled from canopy height, ground elevation, incidence angle, and baseline information using the RVoG model presented in (3.4). All model parameters have been chosen to be normally distributed random variables, with statistics either estimated from training data or appropriately chosen based on the experience from earlier studies. Polarimetric coherence is modelled as a normally distributed random variable. The polarimetric phase difference has been found correlated with biomass and it is modelled using a linear function with an additive, zero-mean Gaussian noise term.

The model performance is evaluated in a side-by-side comparison of the modelled SAR images with the SAR images acquired by the E-SAR system. The same acquisition as used for model training is used in this evaluation. It is concluded that accurate modelling is achieved with the FM for the HH- and HV-polarised backscatter, the interferometric phase differences, and the polarimetric phase difference. However, modelling of the VV-polarised backscatter coefficient, the polarimetric coherence, and the interferometric coherences need to be studied further, as not all structures can be reproduced from the input data using the presented model.

In Figure 4.2, the results from backscatter modelling of the HV- and VV-channels from biomass are shown. Good agreement with the reference E-SAR image is observed for the HV-channel, where the correlation with biomass is high.

4.3 Paper B

In this paper, a new biomass retrieval model is presented. The model includes terms which partially compensate for the influence of topographic and moisture variations. The model is evaluated on E-SAR data acquired in both Remningstorp and Krycklan. The model has been developed within the BIOMASS feasibility study and it has been included in the proposed biomass estimation algorithm for boreal forests [3].

The model is based on the power law function shown in (3.1), together with the backscatter ratio between the HH- and VV-channels, which has been found less susceptible to topographic and moisture variations, due to the often similar influence of these two effects on both co-polarised channels. A topographic correction is also included in the model:

$$\log_{10}\mathcal{B} = a_0 + a_1[\gamma^0_{\mathrm{HV}}]_{\mathrm{dB}} + (a_2 + a_3\theta_g)\left[\frac{\gamma^0_{\mathrm{HH}}}{\gamma^0_{\mathrm{VV}}}\right]_{\mathrm{dB}}, \tag{4.4}$$

where a_0, a_1, a_2, and a_3 are model parameters estimated from the training data and θ_g is the ground slope.

The model is evaluated together with five other models in a set of tests using the E-SAR data from the BioSAR 2007 and 2008 campaigns. The data have been acquired in different test sites, at different flight headings, and in different moisture

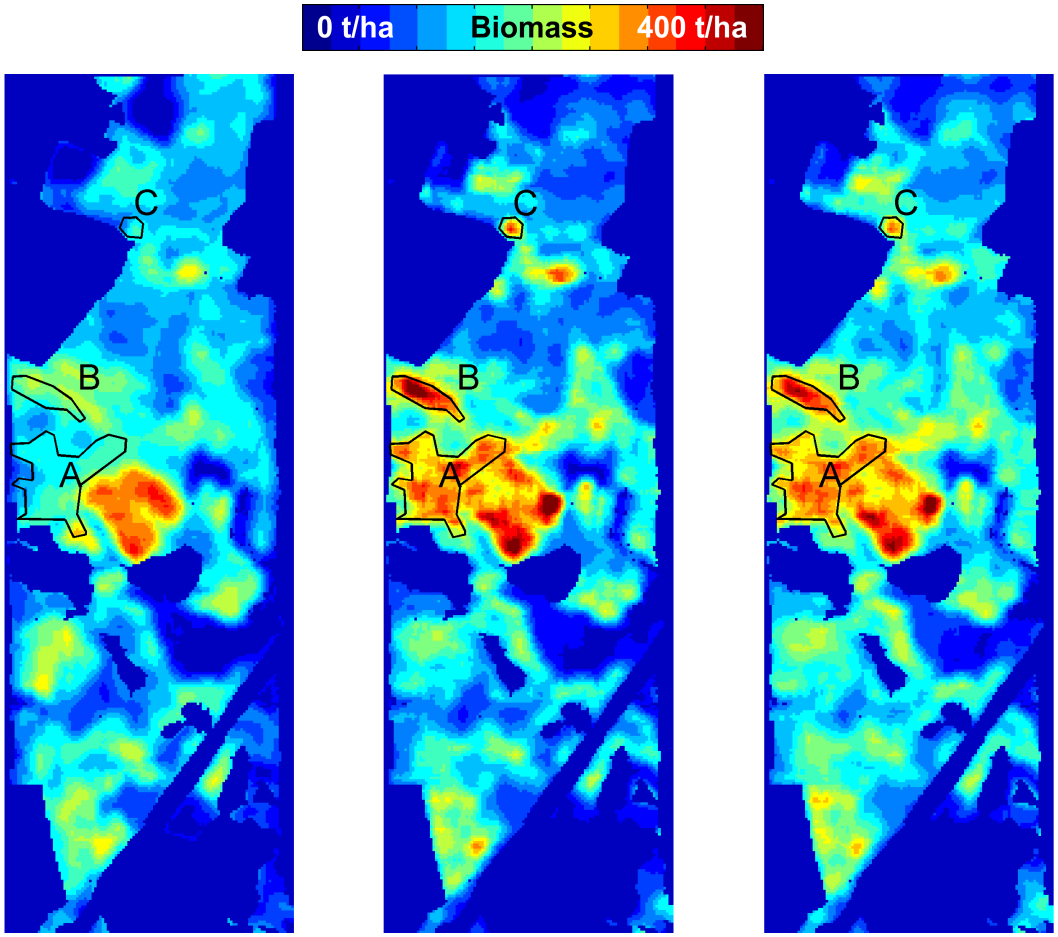

(a) Reference (lidar) (b) Estimated (E-SAR, Re) (c) Estimated (E-SAR, Kr)

Figure 4.3: In Paper B, biomass is estimated from P-band SAR backscatter using a new model with topographic and moisture correction. Three biomass maps for Remningstorp are here shown, estimated from: (a) lidar data, (b) SAR data, using the new model with parameters estimated in Remningstorp, and (c) SAR data, using the new model with parameters estimated in Krycklan, which is 720 km north-north-east of Remningstorp. Regions A, B, and C mark some disagreements, which are discussed in the text.

---

conditions. By using across-acquisition and across-site evaluation scenarios, it is possible to evaluate model susceptibility to topographic and moisture variations, as well as the potential of using the same parameter setup in different conditions.

It is concluded that the proposed model, with parameters estimated in Krycklan, can be used to estimate biomass in Remningstorp with a root-mean-square error of 40–59 tons/ha, or 22–32% of the mean biomass, which is significantly better compared

to the other models. Since the two test sites are separated by 720 km and they feature quite different types of boreal forests, this is a very important conclusion for the future global mission.

In Figure 4.3, biomass maps of Remningstorp, estimated using the proposed model with two parameter sets, one for Remningstorp and one for Krycklan, and compared to a reference biomass map estimated from lidar data. The performance is generally good, although some disagreements with respect to the lidar-based map can be observed. In region A, a significant understorey vegetation layer causes an increased HV backscatter, without contributing significantly to the total biomass. The disagreement in region B is caused both by an overestimation of biomass in the SAR map due to a strong double-bounce effect present in the HV-channel, and by an underestimation of biomass in the reference lidar data. The disagreement in region C is caused by an unusually strong double-bounce effect occurring for a group of tall trees surrounded by lower forest.

4.4 Paper C

In this paper, an approach based on the IWCM and developed for stem volume retrieval from repeat-pass interferometric, C-band ERS-1/2 data is used for biomass retrieval from single-pass interferometric, X-band TanDEM-X data, which have been ground-corrected using a high-resolution DTM. Multi-temporal data are studied, and the influence of both acquisition geometry and meteorological variables is assessed.

The development of an InSAR processing algorithm was an important part of the work conducted for this paper. Due to the quasi-bistatic acquisition geometry with one transmitting and two receiving satellites, and the helical orbit with dynamic baseline, a dedicated InSAR processing algorithm was developed for the TanDEM-X data. Using satellite state vectors, a geocoding look-up table was computed, and the high-resolution DTM was interpolated to radar geometry. The raw interferograms were then ground-corrected using the interpolated DTM and taking into consideration the quasi-bistatic acquisition geometry and satellite displacement between transmission and reception of the signals. A 5-metre buffer zone was added prior to plot- and stand-level averaging. Phase estimation errors were minimised by complex averaging of all relevant pixels within each plot/stand. Absolute phase calibration was done using ground reference points derived from a non-forest mask. Phase unwrapping was found unnecessary due to the limited height variations in the flattened interferogram. Conversion to height was done using a HOA map computed from the acquisition geometry. Geocoding and height estimation accuracies were evaluated using two 5-metre trihedral corner reflectors positioned within the Remningstorp test site. The standard deviation of height variations was found lower than 10 cm and the horizontal offset was found lower than 2 m.

In this study, the IWCM is compared to two other models, each being its simplified version: the RVoG, in which canopy gaps are neglected, and a new penetration depth (PD) model, in which both canopy gaps and ground contribution are neglected. The

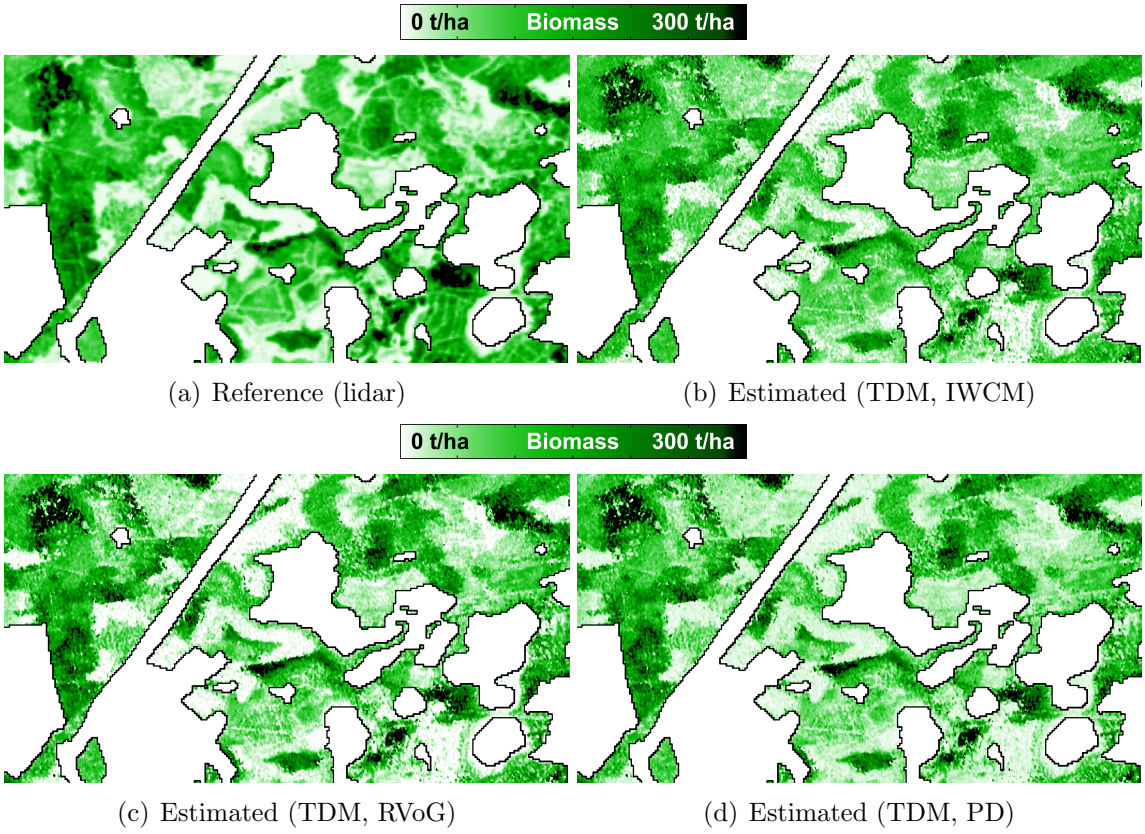

(a) Reference (lidar) (b) Estimated (TDM, IWCM)

(c) Estimated (TDM, RVoG) (d) Estimated (TDM, PD)

Figure 4.4: In Paper C, biomass is estimated using three models: IWCM, RVoG, and a new penetration depth (PD) model. Above, the corresponding maps are compared to a lidar-derived reference map. The test site is Remningstorp and non-forested areas have been masked out. Note that there is one year time difference between the TanDEM-X (TDM) and lidar acquisitions, and growth and forest management have not been accounted for (e.g., in the cleared area slightly to the left from the bottom right corner of the images). The original TDM data have been acquired on 2011-06-04, with a HOA of 49 m, and at an incidence angle of 41°.

---

models are fitted to both intensity, coherence, and phase centre height data, and biomass is estimated.

The new PD model is a simplification valid for dense forests, and it requires one single parameter, the penetration depth, which is used to compensate the phase centre height for penetration. The compensated height is then converted to biomass using a height-to-biomass relation:

$$\mathcal{B} = 0.21 \left(h_{\mathrm{gc}} + \frac{1}{\alpha} \right)^{2.17}, \tag{4.5}$$

where the biomass $\mathcal{B}$ is measured in tons per hectare, h_{gc} is the phase centre elevation

above ground (in metres) and α is the effective extinction coefficient (in m^{-1}).

The models are evaluated using eighteen VV-polarised TanDEM-X image pairs acquired over Remningstorp between 2011-06-04 and 2012-08-24, at HOAs between 49 m and 358 m, incidence angles between 34° and 41°, and in both ascending and descending modes. High-resolution DTM acquired within a national lidar scanning campaign is used as ground reference during InSAR processing. Meteorological data provided by the Swedish Meteorological and Hydrological Institute (SMHI) are also used in the study. The retrieval performance is assessed using 201 forest stands with a minimum size of 1 ha, and biomass in the interval 6–267 t/ha (mean: 105 t/ha), equally divided into two groups: one for training and one for validation. The root-mean-square error (RMSE) for the IWCM-based retrieval is between 17% and 33%, with the best results obtained for the low HOAs. For the RVoG and the PD models, the stand-level RMSE values are slightly higher. Biomass is also estimated using multi-temporal averaging from all eighteen acquisitions with a weighting factor inversely proportional to the square of HOA, with an RMSE of 16% and $R^2 = 0.93$.

In Figure 4.4, biomass maps obtained with each of the three models for an image from 2011-06-04 with a HOA of 49 m and an incidence angle of 41° are compared to a reference map estimated from lidar data. Good results are obtained for all models, except in the region that has been harvested between the lidar and SAR acquisitions.

4.5 Paper D

In this paper, the two-level model (TLM) is introduced and used for the estimation of forest height and canopy density from single-polarised TanDEM-X acquisitions in combination with a high-resolution DTM. With an access to the global TanDEM-X data, the presented approach can be used for frequent, large-scale, high-resolution mapping of forest height and canopy density in countries in which national lidar scanning campaigns have been conducted.

The TLM models forest as two discrete scattering levels: ground and vegetation, separated by a distance Δh and with canopy gaps described by the area-fill factor η, which is the fraction of the total area covered by the vegetation level. The two-level approach with canopy gaps is motivated by an interference effect observed in the data for sparse forest plots, for which the location of the scattering centre in the canopy is found sensitive to the interferometric baseline.

The ground-corrected complex correlation coefficient is modelled by the TLM as:

$$\tilde{\gamma}_{\mathrm{gc}} = \frac{\mu + e^{ik_z \Delta h}}{\mu + 1}, \tag{4.6}$$

where μ the area-weighted backscatter ratio:

$$\mu = \frac{\sigma^0_{\mathrm{gr}}}{\sigma^0_{\mathrm{veg}}} \frac{1-\eta}{\eta}. \tag{4.7}$$

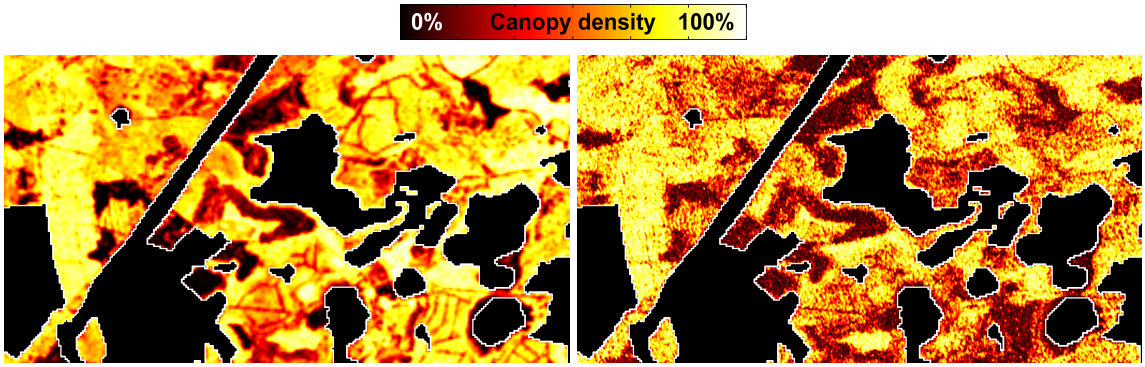

(a) Reference (lidar vegetation ratio) (b) Estimated (uncorrected area-fill factor η_0)

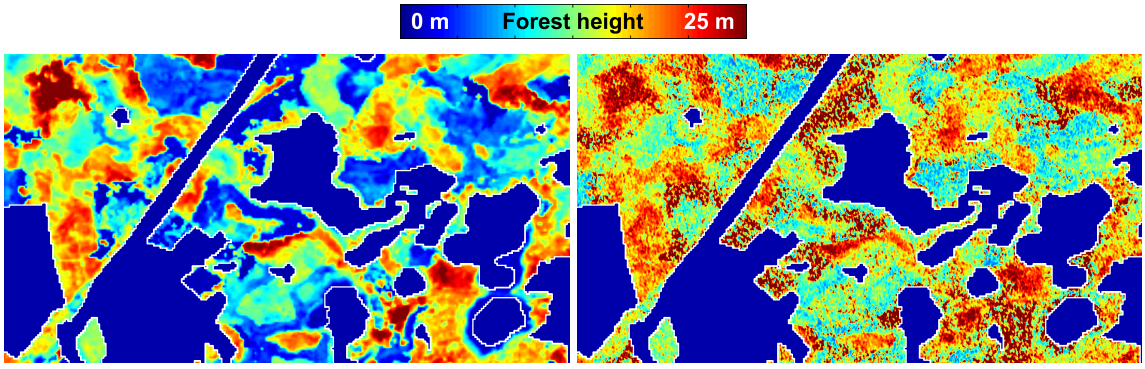

(c) Reference (lidar height H50) (d) Estimated (level distance Δh)

Figure 4.5: In Paper D, forest height and canopy density are estimated from the inversion of the TLM. Above, the corresponding maps are compared to lidar-derived reference maps. The test site is Remningstorp and non-forested areas have been masked out. Note that there is one year time difference between the TDM and lidar acquisitions, and growth and forest management have not been accounted for (e.g., in the cleared area slightly to the left from the bottom right corner of the images). The original TDM data have been acquired on 2011-06-04, with a HOA of 49 m, and at an incidence angle of 41°.

As the TLM requires only two parameters (Δh and μ), model inversion can be done individually for each ground-corrected complex correlation coefficient, without the need for additional SAR acquisitions. Analytical expressions for the computation of Δh and μ from a ground-corrected complex correlation coefficient are presented in the paper.

The model is evaluated using eight VV-polarised TanDEM-X acquisitions made at different baselines (HOAs between 32 and 63 metres) over Remningstorp in the summers of 2011, 2012, and 2013, and thirty-two, 0.5 hectare circular forest plots with different heights and canopy densities. The InSAR data have been processed

using the same InSAR processing algorithm as described in Paper C.

It is concluded that level distance Δh can be used as an estimate of H50 (50th percentile of all lidar returns above 1 m or 10% of the maximal height) with a Pearson correlation coefficient of about 95% and a root-mean-square difference (RMSD) lower than 10% (or 1.8 m). It is also concluded that the uncorrected area-fill factor:

$$\eta_0 = \frac{1}{1+\mu} \tag{4.8}$$

can be used as an estimate of the vegetation ratio (the ratio between the number of lidar returns from above 1 m or 10% of the maximal height and all lidar returns) with a Pearson correlation coefficient better than 59% and RMSD around 10% (or 0.07). A HOA-dependent offset is observed for Δh, and it is most likely caused by residual SNR and system decorrelation effects, which have not been compensated for.

In Figure 4.5, maps of Δh and η_0 obtained from TLM inversion of a TanDEM-X acquisition from 2011-06-04 with a HOA of 49 metres and an incidence angle of 41° are compared to maps of H50 and VR, derived from lidar data acquired one year earlier. Forest changes such as growth and forest management procedures have not been accounted for.

4.6 Paper E

In this paper, biomass is estimated from forest height and canopy density estimates obtained from the inversion of the TLM presented in Paper D. With an access to the global TanDEM-X data, the presented approach can be used for frequent, large-scale, high-resolution mapping of biomass in countries in which national lidar scanning campaigns have been conducted.

The introduced TLM biomass model (TBM) is a power law function of the level distance Δh and the uncorrected area-fill factor η_0 obtained from TLM inversion:

$$\mathcal{B} = K \Delta h^{\alpha} \eta_0^{\beta}, \tag{4.9}$$

where $\mathcal{B}$ is the biomass in tons per hectare, and K, α, and β are model parameters. The power law form of the model is motivated by similar functions used in lidar-based biomass mapping.

The model is evaluated using eighteen VV-polarised TanDEM-X acquisitions made at different baselines (HOAs between 32 and 63 metres) over both Remningstorp and Krycklan in the summers of 2011, 2012, and 2013. Eight of these images have been used in the study summarised in Paper D. In Remningstorp, between 32 and 21 forest plots are used, whereas in Krycklan, 29 forest stands are used. The TBM is compared to a zero-intercept, linear scaling model (SM), in which biomass is estimated from a direct scaling of the ground-corrected interferometric height, as proposed in [172]. The models are evaluated in across-acquisition and across-site scenarios, to assess their operational values.

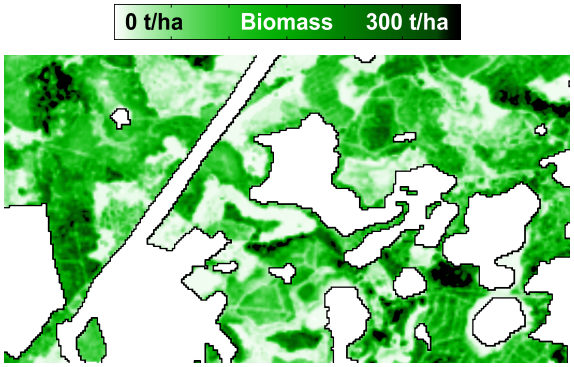

(a) Reference (lidar)

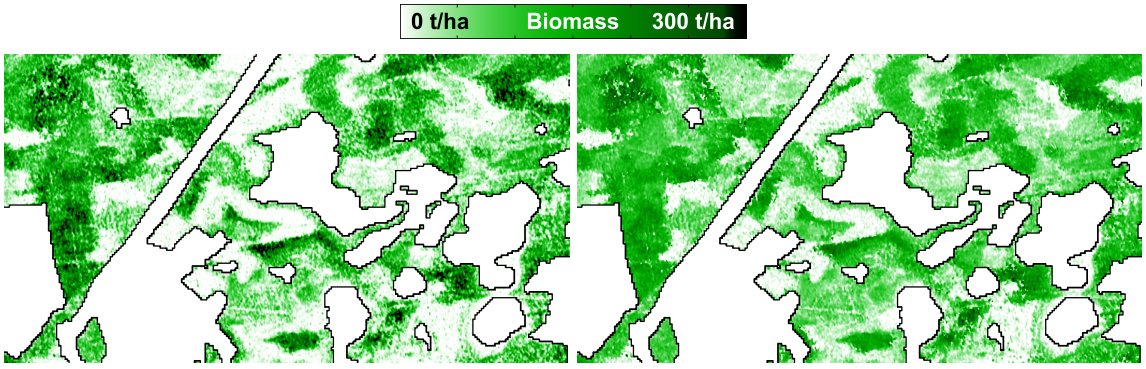

(b) Estimated (TDM, TBM) (c) Estimated (TDM, SM)

Figure 4.6: In Paper E, biomass is estimated from forest height and canopy density estimates obtained from TLM inversion using the TLM biomass model (TBM), and compared to a scaling model (SM), which scales the ground-corrected interferometric height to biomass, as proposed in [172]. Above, the corresponding maps are compared to a lidar-derived reference map. The test site is Remningstorp and non-forested areas have been masked out. Note that there is one year time difference between the TDM and lidar acquisitions, and growth and forest management have not been accounted for (e.g., in the cleared area slightly to the left from the bottom right corner of the images). The original TDM data have been acquired on 2011-06-04, with a HOA of 49 m, and at an incidence angle of 41°.

The TBM can explain between 65% and 89% of the AGB variance observed in the data, with a residual root-mean-square error (RMSE) in the interval 12–19% (median: 15%). If model training and validation are carried out on different TanDEM-X acquisitions or different test sites, the prediction RMSE increases (12–80%, median: 30%). With α fixed and β a site-dependent constant, the prediction RMSE is lower (12–56%, median: 17%), while the residual RMSE is similar (12-29%, median: 16%). The SM shows similar performance when used on Krycklan data, whereas for Remningstorp

data and across-site retrieval, the performance is poorer.

In general, the retrieval performance of the TBM with fixed α and β is good, with an RMSE below 20% for all acquisitions in Krycklan and for almost all acquisitions in Remningstorp with HOA above 40 m. In Remningstorp, where the forest is generally taller and with more complex horizontal structure (due to management), the performance of the model is decreased at HOAs below 40 m, where the errors caused by the insufficient modelling of the vertical structure have the strongest impact. It is also observed that the HOA-dependent offset in Δh, noted earlier in Paper D and most likely caused by the lack of SNR and system decorrelation modelling, causes reduced performance of the biomass model at low HOAs. A coherence calibration step is therefore proposed for the future.

In Figure 4.6, a biomass map for Remningstorp, estimated with the TBM using the forest height and canopy density estimates shown in Figure 4.5, is compared to a reference biomass map estimated from lidar data, and a biomass map created using the scaling model (SM), in which biomass is computed by scaling from the ground-corrected interferometric height (h_{gc}). The TBM-based estimate is better, as it is able to reproduce the full biomass variance. Note that the time difference between lidar and SAR acquisitions is one year, and forest changes such as growth and forest management procedures have not been accounted for.

Chapter 5

Conclusions

The main scope of the work conducted for this thesis has been to develop methods for forest parameter estimation from SAR imagery. By using P- and X-band, i.e., the lowest and highest frequency bands available and useful for spaceborne imaging of the Earth, this task has been studied in both the low- and high-frequency regimes.

Both empirical and theoretical models linking forest parameters to polarimetric and interferometric SAR observables have been developed. Within the models, some effects previously unaccounted for have been included. At P-band, an improved biomass retrieval model has been developed by including empirical corrections for the topographic and moisture variations. At X-band, the estimation of biomass has been improved and the estimation of canopy density has been made possible by introducing a model in which canopy gaps are used to explain volume decorrelation.

The models have been developed with their operational values in mind. At P-band, the proposed biomass model requires one single polarimetric acquisition, which is expected to be the standard acquisition mode for BIOMASS, and a ground slope map, which most likely can be derived from a standard TanDEM-X DEM. It has also been shown that the proposed model can be used in two geographically distant test sites with the same parameter setup, which reduces the requirements on training data.

At X-band, the proposed TLM inversion yields estimates of forest height and canopy density, and it can be performed using single-polarised TanDEM-X acquisitions, e.g., from the existing global data set, provided that a high-resolution digital terrain

model (DTM) is available. With the temporal stability of the ground in most forested regions, the increasing popularity of national lidar scanning campaigns, and the upcoming P- and L-band InSAR missions (BIOMASS, and possibly also SAOCOM-CS and TanDEM-L), the availability of high-resolution DTMs will increase with time. The proposed biomass model requires local estimation of only one parameter related to canopy density, whereas the other parameters can be fixed for the two studied test sites, which reduces the requirements on training data.

5.1 Thesis Highlights

At P-band, the following findings can be considered the highlights of this thesis:

- The HH/VV backscatter ratio has been found useful for the compensation of topographic and moisture variations, which often have similar impact on the two co-polarised channels, and their influence is decreased when the ratio is formed.
- It has been shown that the same biomass model can be used with the same parameter values in both Remningstorp and Krycklan, which are two test sites separated by 720 km and featuring different types of boreal forest, due to the large contribution of tree trunks to the total backscatter.

At X-band, the most interesting findings can be summarised in the following highlights:

- For sparse plots with low canopy density, the location of the scattering phase centre has been found sensitive to the baseline. This is explained by an interference effect occurring when ground- and canopy-level contributions are of similar strength.
- The contribution of canopy gaps has been found significant at X-band, as shown in a comparative study of the three models: IWCM, RVoG, and a penetration depth model. Moreover, direct inversion of a two-level model (TLM), in which forest is modelled as two scattering levels and penetration can only occur through canopy gaps, can provide estimates of both forest height and canopy density.
- Biomass can be accurately estimated from forest height and canopy density estimates obtained from the inversion of the TLM using a power law model. However, the same exponent for the canopy density estimate cannot be used in both Remningstorp and Krycklan, due to the large difference in canopy structure.

5.2 Future Prospects

There are several topics that need to be studied in the future to further improve the results presented in this thesis. For all studies, one of the most important extensions

is to apply the presented approaches on other data sets (other biomes, acquisition geometries, frequencies), in order to evaluate the generality of the findings and further improve the understanding of the governing processes.

At P-band, one of the largest difficulties encountered during forest parameter estimation is the influence of topographic and moisture variations on the backscattered signal, which is to a large degree still unknown. The forward model presented in Paper A does not account for these effects, and the biomass retrieval model presented in Paper B includes empirical correction terms, the HH/VV-ratio and the surface slope, which only partially compensate for these effects. Theoretical modelling is needed for better understanding of the scattering processes, for example using cylinder over ground models. Moreover, as noted in Paper A, the modelling of the interferometric coherence also needs to be improved, for example by using other vertical scattering profiles, or by improved modelling of the RVoG parameters. The inclusion of canopy gaps in P-band modelling should also be evaluated. Finally, the observed correlation between the HH-VV phase difference and biomass needs to be studied further using theoretical models. Also, its potential for biomass estimation needs to be evaluated.

At X-band, the TLM-based methods for forest height, canopy density, and biomass estimation are currently based on the assumptions of known topography, and negligible SNR and system decorrelation effects. Consequently, the first assumption makes the current approach unfeasible in regions with unknown topography, and the latter assumption introduces a HOA-dependent offset in regions with low volume decorrelation, as observed in Papers D and E. It would be interesting to extend the current model to the multi-polarised case and evaluate the possibility of reducing these requirements. Also, the inclusion of a coherence calibration step in the processing chain may improve TLM inversion performance in lower forests, and the HOA-dependent offset may be reduced. Additionally, the TLM inversion may be applied on multi-temporal and/or multi-baseline data, making it possible to study forest change and/or forest structure. The influence of meteorological conditions needs to be studied.

References

[1] World Wide Fund for Nature (WWF). Forests, jungles, woods & their trees. Retrieved from: http://wwf.panda.org/about_our_earth/about_forests/ (2014-08-08).

[2] C. Parker, A. Mitchell, M. Trivedi, and N. Mardas, *The Little REDD Book: A guide to governmental and non-governmental proposals for reducing emissions from deforestation and degradation*. Global Canopy Programme, John Krebs Field Station, Oxford OX2 8QJ, UK, 2008.

[3] ESA (2012), *Report for Mission Selection: BIOMASS*, ESA SP-1324/1 (3 volume series), European Space Agency, Noordwijk, The Netherlands.

[4] E. Næsset, T. Gobakken, S. Solberg, T. G. Gregoire, R. Nelson, G. Ståhl, and D. Weydahl, "Model-assisted regional forest biomass estimation using lidar and InSAR as auxiliary data: A case study from a boreal forest area," *Remote Sensing of Environment*, vol. 115, no. 12, pp. 3599–3614, 2011.

[5] B. Koch, "Status and future of laser scanning, synthetic aperture radar and hyperspectral remote sensing data for forest biomass assessment," *ISPRS Journal of Photogrammetry and Remote Sensing*, vol. 65, no. 6, pp. 581–590, 2010.

[6] A. Moreira, P. Prats-Iraola, M. Younis, G. Krieger, I. Hajnsek, and K. Papathanassiou, "A tutorial on synthetic aperture radar," *IEEE Geoscience and Remote Sensing Magazine*, vol. 1, no. 1, pp. 6–43, 2013.

[7] K. J. Ranson, G. Sun, R. H. Lang, N. S. Chauhan, R. J. Cacciola, and O. Kilic, "Mapping of boreal forest biomass from spaceborne synthetic aperture radar," *Journal of Geophysical Research*, vol. 102, pp. 29 599–29 610, 1997.

[8] H. Israelsson, L. M. H. Ulander, J. I. H. Askne, J. E. S. Fransson, P.-O. Frölind, A. Gustavsson, and H. Hellsten, "Retrieval of forest stem volume using VHF SAR," *IEEE Transactions on Geoscience and Remote Sensing*, vol. 35, no. 1, pp. 36–40, 1997.

[9] H. Israelsson, "SAR remote sensing of forests from microwaves to VHF," Ph.D. dissertation, Chalmers University of Technology, 1998.

[10] F. Walter, "Extraction of forest tree volume from CARABAS SAR data," *Scandinavian Journal of Forest Research*, vol. 12, no. 4, pp. 370–374, 1997.

[11] J. E. S. Fransson, F. Walter, and L. M. H. Ulander, "Estimation of forest parameters using CARABAS-II VHF SAR data," *IEEE Transactions on Geoscience and Remote Sensing*, vol. 38, no. 2, pp. 720–727, 2000.

[12] G. Smith and L. M. H. Ulander, "A model relating VHF-band backscatter to stem volume of coniferous boreal forest," *IEEE Transactions on Geoscience and Remote Sensing*, vol. 38, no. 2, pp. 728–740, 2000.

[13] G. Smith, "Radar remote sensing of forests using CARABAS and ERS," Ph.D. dissertation, Chalmers University of Technology, 2000.

[14] P. Melon, J. M. Martinez, T. Le Toan, L. M. H. Ulander, and A. Beaudoin, "On the retrieving of forest stem volume from VHF SAR data: Observation and modelling," *IEEE Transactions on Geoscience and Remote Sensing*, vol. 39, no. 11, pp. 2364–2372, 2001.

[15] J. E. S. Fransson, G. Smith, F. Walter, A. Gustavsson, and L. M. H. Ulander, "Estimation of forest stem volume in sloping terrain using CARABAS-II VHF SAR data," *Canadian Journal of Remote Sensing*, vol. 30, no. 4, pp. 651–660, 2004.

[16] B. Hallberg, G. Smith-Jonforsen, and L. M. H. Ulander, "Measurements on individual trees using multiple VHF SAR images," *IEEE Transactions on Geoscience and Remote Sensing*, vol. 43, no. 10, pp. 2261–2269, 2005.

[17] G. Smith-Jonforsen, L. M. H. Ulander, and X. Luo, "Low VHF-band backscatter from coniferous forests on sloping terrain," *IEEE Transactions on Geoscience and Remote Sensing*, vol. 43, no. 10, pp. 2246–2260, 2005.

[18] A. A. Kononov and M.-H. Ka, "Model-associated forest parameter retrieval using VHF SAR data at the individual tree level," *IEEE Transactions on Geoscience and Remote Sensing*, vol. 46, no. 1, pp. 69–84, 2008.

[19] B. Hallberg, "Synthetic-aperture radar imaging of forests in the VHF and UHF bands: Electromagnetic models and data analysis," Ph.D. dissertation, Chalmers University of Technology, 2007.

[20] K. Folkesson, G. Smith-Jonforsen, and L. M. H. Ulander, "Validating backscatter models for CARABAS SAR images of coniferous forests," *Canadian Journal of Remote Sensing*, vol. 34, no. 5, pp. 480–495, 2008.

[21] K. Folkesson, "Model-based stem volume retrieval and widthrow detection using CARABAS and P-band SAR," Ph.D. dissertation, Chalmers University of Technology, 2008.

[22] K. Folkesson, G. Smith-Jonforsen, and L. M. H. Ulander, "Model-based compensation of topographic effects for improved stem-volume retrieval from CARABAS-II VHF-band SAR images," *IEEE Transactions on Geoscience and Remote Sensing*, vol. 47, no. 4, pp. 1045–1055, 2009.

[23] M. Moghaddam, Y. Rahmat-Samii, E. Rodriguez, D. Entekhabi, J. Hoffman, D. Moller, L. E. Pierce, S. Saatchi, and M. Thomson, "Microwave Observatory of Subcanopy and Subsurface (MOSS): A mission concept for global deep soil moisture observations," *IEEE Transactions on Geoscience and Remote Sensing*, vol. 45, no. 8, pp. 2630–2643, 2007.

[24] T. Le Toan, A. Beaudoin, J. Riom, and D. Guyon, "Relating forest biomass to SAR data," *IEEE Transactions on Geoscience and Remote Sensing*, vol. 30, no. 2, pp. 403–411, 1992.

[25] M. C. Dobson, F. T. Ulaby, T. Le Toan, A. Beaudoin, E. S. Kasischke, and N. Christensen, "Dependence of radar backscatter on coniferous forest biomass," *IEEE Transactions on Geoscience and Remote Sensing*, vol. 30, no. 2, pp. 412–415, 1992.

[26] A. Beaudoin, T. Le Toan, S. Goze, E. Nezry, A. Lopes, E. Mougin, C. C. Hsu, H. C. Han, J. A. Kong, and R. T. Shin, "Retrieval of forest biomass from SAR data," *International Journal of Remote Sensing*, vol. 15, no. 14, pp. 2777–2796, 1994.

[27] H. Israelsson, J. Askne, and R. Sylvander, "Potential of SAR for forest bole volume estimation," *International Journal of Remote Sensing*, vol. 15, no. 14, pp. 2809–2826, 1994.

[28] K. J. Ranson and G. Sun, "Mapping biomass of a northern forest using multifrequency SAR data," *IEEE Transactions on Geoscience and Remote Sensing*, vol. 32, no. 2, pp. 388–396, 1994.

[29] Y. Rauste, T. Häma, J. Pulliainen, K. Heiska, and M. Hallikainen, "Radar-based forest biomass estimation," *International Journal of Remote Sensing*, vol. 15, no. 14, pp. 1797–2808, 1994.

[30] M. L. Imhoff, "Radar backscatter and biomass saturation: Ramifications for global biomass inventory," *IEEE Transactions on Geoscience and Remote Sensing*, vol. 33, no. 2, pp. 511–518, 1995.

[31] E. J. Rignot, R. Zimmermann, and J. J. van Zyl, "Spaceborne applications of P band imaging radars for measuring forest biomass," *IEEE Transactions on Geoscience and Remote Sensing*, vol. 33, no. 5, pp. 1162–1169, 1995.

[32] D. H. Hoekman and M. J. Quiñones, "Land cover type and biomass classification using AirSAR data for evaluation of monitoring scenarios in the

Colombian Amazon," *IEEE Transactions on Geoscience and Remote Sensing*, vol. 38, no. 2, pp. 685–696, 2000.

[33] J. R. Santos, C. C. Freitas, L. S. Araujo, L. V. Dutra, J. C. Mura, F. F. Gama, L. S. Soler, and S. J. S. Sant'Anna, "Airborne P-band SAR applied to the aboveground biomass studies in the Brazilian tropical rainforest," *Remote Sensing of Environment*, vol. 87, no. 4, pp. 482–493, 2003.

[34] G. Smith-Jonforsen, K. Folkesson, B. Hallberg, and L. M. H. Ulander, "Effects of forest biomass and stand consolidation on P-band backscatter," *IEEE Geoscience and Remote Sensing Letters*, vol. 4, no. 4, pp. 669–673, 2007.

[35] S. Saatchi, K. Halligan, D. Despain, and R. Crabtree, "Estimation of forest fuel load from radar remote sensing," *IEEE Transactions on Geoscience and Remote Sensing*, vol. 45, no. 6, pp. 1726–1740, 2007.

[36] G. Sandberg, L. M. H. Ulander, J. E. S. Fransson, J. Holmgren, and T. Le Toan, "L- and P-band backscatter intensity for biomass retrieval in hemiboreal forest," *Remote Sensing of Environment*, vol. 115, no. 11, pp. 2874–2886, 2011.

[37] S. Saatchi, M. Marlier, R. L. Chazdon, D. B. Clark, and A. E. Russell, "Impact of spatial variability of tropical forest structure on radar estimation of aboveground biomass," *Remote Sensing of Environment*, vol. 115, no. 11, pp. 2836–2849, 2011.

[38] T. Le Toan, S. Quegan, M. W. J. Davidson, H. Balzter, P. Paillou, K. Papathanassiou, S. Plummer, F. Rocca, S. Saatchi, H. Shugart, and L. M. H. Ulander, "The BIOMASS mission: Mapping global forest biomass to better understand the terrestrial carbon cycle," *Remote Sensing of Environment*, vol. 115, no. 11, pp. 2850–2860, 2011.

[39] M. Neumann, S. S. Saatchi, L. M. H. Ulander, and J. E. S. Fransson, "Assessing performance of L- and P-band polarimetric interferometric SAR data in estimating boreal forest above-ground biomass," *IEEE Transactions on Geoscience and Remote Sensing*, vol. 50, no. 3, pp. 714–726, 2012.

[40] G. Sandberg, "Estimation of forest biomass and Faraday rotation using ultra high frequency synthetic aperture radar," Ph.D. dissertation, Chalmers University of Technology, 2013.

[41] I. Hajnsek, R. Scheiber, L. M. H. Ulander, A. Gustavsson, G. Sandberg, S. Tebaldini, A. M. Guarnieri, F. Rocca, F. Bombardini, and M. Pardini, "BioSAR 2007 technical assistance for the development of airborne SAR and geophysical measurements during the BioSAR 2007 experiment: Final report without synthesis," ESA contract no. 20755/07/NL/CB, Tech. Rep., 2008.

[42] L. M. H. Ulander, A. Gustavsson, B. Flood, D. Murdin, P. Dubois-Fernandez, X. Depuis, G. Sandberg, M. J. Soja, L. E. B. Eriksson, J. E. S. Fransson, J. Holmgren, and J. Wallerman, "BioSAR 2010: Technical assistance for the development of airborne SAR and geophysical measurements during the BioSAR 2010 experiment: Final report," ESA contract no. 4000102285/10/NL/JA/ef, Tech. Rep., 2011.

[43] P. C. Dubois-Fernandez, T. Le Toan, S. Daniel, H. Oriot, J. Chave, L. Blanc, L. Villard, M. Davidson, and M. Petit, "The TropiSAR airborne campaign in French Guiana: Objectives, description, and observed temporal behavior of the backscatter signal," *IEEE Transactions on Geoscience and Remote Sensing*, vol. 50, no. 8, pp. 3228–3241, 2012.

[44] F. Garestier, P. C. Dubois-Fernandez, and I. Champion, "Forest height inversion using high-resolution P-band Pol-InSAR data," *IEEE Transactions on Geoscience and Remote Sensing*, vol. 46, no. 11, pp. 3544–3559, 2008.

[45] I. Hajnsek, F. Kugler, S.-K. Lee, and K. P. Papathanassiou, "Tropical-forest-parameter estimation by means of Pol-InSAR: The INDREX-II campaign," *IEEE Transactions on Geoscience and Remote Sensing*, vol. 47, no. 2, pp. 481–493, 2009.

[46] F. Garestier, P. C. Dubois-Fernandez, D. Guyon, and T. Le Toan, "Forest biophysical parameter estimation using L- and P-band polarimetric SAR data," *IEEE Transactions on Geoscience and Remote Sensing*, vol. 47, no. 10, pp. 3379–3388, 2009.

[47] S. Tebaldini and F. Rocca, "Multibaseline polarimetric SAR tomography of a boreal forest at P- and L-bands," *IEEE Transactions on Geoscience and Remote Sensing*, vol. 50, no. 1, pp. 232–246, 2012.

[48] D. H. T. Minh, T. L. Toan, F. Rocca, S. Tebaldini, M. d'Alessandro, and L. Villard, "Relating P-band synthetic aperture radar tomography to tropical forest biomass," *IEEE Transactions on Geoscience and Remote Sensing*, vol. 52, no. 2, pp. 967–979, 2014.

[49] N. C. Rogers, S. Quegan, J. S. Kim, and K. P. Papathanassiou, "Impacts of ionospheric scintillation on the BIOMASS P-band satellite SAR," *IEEE Transactions on Geoscience and Remote Sensing*, vol. 52, no. 3, pp. 1856–1868, 2014.

[50] N. C. Rogers and S. Quegan, "The accuracy of Faraday rotation estimation in satellite synthetic aperture radar images," *IEEE Transactions on Geoscience and Remote Sensing*, vol. 52, no. 8, pp. 4799–4807, 2014.

[51] F. Heliere, F. Fois, M. Arcioni, P. Bensi, M. Fehringer, and K. Scipal, "Biomass P-band SAR interferometric mission selected as 7th Earth Explorer Mission,"

in *10th European Conference on Synthetic Aperture Radar (EUSAR)*, Berlin, Germany, 3–5 June 2014, pp. 1152–1155.

[52] P. Lopez-Dekker, F. De Zan, T. Borner, M. Younis, K. Papathanassiou, T. Guardabrazo, V. Bourlon, S. Ramongassie, N. Taveneau, L. M. H. Ulander, D. Murdin, N. Rogers, S. Quegan, and R. Franco, "Biomass end-to-end mission performance simulator," in *IEEE International Geoscience and Remote Sensing Symposium (IGARSS)*, Vancouver, BC, Canada, 24–29 July 2011, pp. 4249–4252.

[53] R. Bamler and P. Hartl, "Synthetic aperture radar interferometry," *Inverse Problems*, vol. 14, pp. R1–R54, 1998.

[54] P. B. G. Dammert, "Spaceborne SAR interferometry: Theory and applications," Ph.D. dissertation, Chalmers University of Technology, 1999.

[55] G. Krieger, A. Moreira, H. Fiedler, I. Hajnsek, M. Werner, M. Younis, and M. Zink, "TanDEM-X: A satellite formation for high-resolution SAR interferometry," *IEEE Transactions on Geoscience and Remote Sensing*, vol. 45, no. 11, pp. 3317–3341, 2007.

[56] T. G. Farr, P. A. Rosen, E. Caro, R. Crippen, R. Duren, S. Hensley, M. Kobrick, M. Paller, E. Rodriguez, L. Roth, D. Seal, S. Shaffer, J. Shimada, J. Umland, M. Werner, M. Oskin, D. Burbank, and D. Alsdorf, "The Shuttle Radar Topography Mission," *Reviews of Geophysics*, vol. 45, no. 2, pp. 1–33, 2007.

[57] J. Askne, P. Dammert, L. M. H. Ulander, and G. Smith, "C-band repeat-pass interferometric SAR observations of the forest," *IEEE Transactions on Geoscience and Remote Sensing*, vol. 35, no. 1, pp. 25–35, 1997.

[58] J. Askne, M. Santoro, G. Smith, and J. E. S. Fransson, "Multitemporal repeat-pass SAR interferometry of boreal forests," *IEEE Transactions on Geoscience and Remote Sensing*, vol. 41, no. 7, pp. 1540–1550, 2003.

[59] S. R. Cloude and K. P. Papathanassiou, "Polarimetric SAR interferometry," *IEEE Transactions on Geoscience and Remote Sensing*, vol. 36, no. 5, pp. 1551–1565, 1998.

[60] K. P. Papathanassiou and S. R. Cloude, "Single-baseline polarimetric SAR interferometry," *IEEE Transactions on Geoscience and Remote Sensing*, vol. 39, no. 11, pp. 2352–2363, 2001.

[61] S. R. Cloude and K. P. Papathanassiou, "Three-stage inversion process for polarimetric SAR interferometry," *IEE Proceedings on Radar, Sonar & Navigation*, vol. 150, no. 3, pp. 125–134, 2003.

[62] J. Praks, O. Antropov, and M. T. Hallikainen, "LIDAR-aided SAR interferomety studies in boreal forest: Scattering phase center and extinction coefficient at X- and L-band," *IEEE Transactions on Geoscience and Remote Sensing*, vol. 50, no. 10, pp. 3831–3843, 2012.

[63] F. Kugler, D. Schulze, I. Hajnsek, H. Pretzsch, and K. P. Papathanassiou, "TanDEM-X Pol-InSAR performance for forest height estimation," *IEEE Transactions on Geoscience and Remote Sensing*, vol. 52, no. 10, pp. 6404–6422, 2014.

[64] N. Gebert, B. Carnicero Dominguez, M. W. J. Davidson, M. Diaz Martin, and P. Silvestrin, "SAOCOM-CS – A passive companion to SAOCOM for single-pass L-band sar interferometry," in *10th European Conference on Synthetic Aperture Radar (EUSAR)*, Berlin, Germany, 3–5 June 2014, pp. 1251–1254.

[65] A. Moreira, G. Krieger, M. Younis, I. Hajnsek, K. Papathanassiou, M. Eineder, and F. De Zan, "Tandem-L: A mission proposal for monitoring dynamic earth processes," in *IEEE International Geoscience and Remote Sensing Symposium (IGARSS)*, Vancouver, BC, Canada, 24–29 July 2011, pp. 1385–1388.

[66] A. Gustavsson, B. Flood, P.-O. Frolind, H. Hellsten, T. Jonsson, B. Larsson, G. Stenstrom, and L. M. H. Ulander, "First airborne tests with the new VHF SAR CARABAS II," in *IEEE International Geoscience and Remote Sensing Symposium (IGARSS)*, Singapore, 3–8 August 1997, pp. 1214–1216.

[67] M. I. Skolnik, *Radar Handbook*, 2nd ed. McGraw-Hill, 1990.

[68] R. J. Sullivan, *Radar Foundations for Imaging and Advanced Concepts*. Scitech Publishing, 2004.

[69] M. A. Richards, J. A. Scheer, and W. A. Holm, Eds., *Principles of Modern Radar, Volume I: Basic Techniques*. Scitech Publishing, 2010.

[70] J. C. Curlander and R. N. McDonough, *Synthetic Aperture Radar: Systems and Signal Processing*. John Wiley & Sons, Inc, 1992.

[71] W. G. Rees, *Physical Principles of Remote Sensing*. Cambridge University Press, 2013.

[72] S. Kingsley and S. Quegan, *Understanding Radar Systems*. McGraw-Hill, 1992.

[73] D. K. Barton, *Radar System Analysis and Modeling*. Artech House, 2005.

[74] "IEEE standard letter designations for radar-frequency bands," *IEEE Std 521-2002 (Revision of IEEE Std 521-1984)*, 2003.

[75] J. Bruder, "IEEE radar standards and the radar systems panel," *IEEE Aerospace and Electronic Systems Magazine*, vol. 28, no. 7, pp. 19–22, 2013.

[76] C. Oliver and S. Quegan, *Understanding Synthetic Aperture Radar Images*. SciTech Publishing, 2004.

[77] R. Jordan, "The Seasat-A synthetic aperture radar system," *IEEE Journal of Oceanic Engineering*, vol. 5, no. 2, pp. 154–164, 1980.

[78] World Meteorological Organisation (WMO). (2014) OSCAR: Observing systems capability analysis and review tool. Retrieved from: http://www.wmo-sat.info/oscar/instrumenttypes/view/23 (2014-09-10).

[79] W. G. Carrara, R. S. Goodman, and R. M. Majewski, *Spotlight Synthetic Aperture Radar: Signal Processing Algorithms*. Artech House, 1995.

[80] W. L. Melvin and J. A. Scheer, Eds., *Principles of Modern Radar, Volume II: Advanced Techniques*. Scitech Publishing, 2013.

[81] F. De Zan and A. Monti Guarnieri, "TOPSAR: Terrain observation by progressive scans," *IEEE Transactions on Geoscience and Remote Sensing*, vol. 44, no. 9, pp. 2352–2360, 2006.

[82] I. G. Cumming and F. H. Wong, *Digital Processing of Synthetic Aperture Radar Data: Algorithms and Implementation*. Artech House, 2005.

[83] C. V. Jakowatz, Jr, D. E. Wahl, P. H. Eichel, D. C. Ghiglia, and P. A. Thompson, *Spotlight-Mode Synthetic Aperture Radar: A Signal Processing Approach*. Springer, 1996.

[84] M. Soumekh, *Synthetic Aperture Radar Signal Processing with MATLAB Algorithms*. Wiley-Interscience, 1999.

[85] A. F. Yegulalp, "Fast backprojection algorithm for synthetic aperture radar," in *IEEE Radar Conference*, Waltham, MA, USA, 20–22 April 1999, pp. 60–65.

[86] L. M. H. Ulander, H. Hellsten, and G. Stenström, "Synthetic-aperture radar processing using fast factorized back-projection," *IEEE Transactions on Aerospace and Electronic Systems*, vol. 39, no. 3, pp. 760–776, 2003.

[87] L. M. H. Ulander and J. O. Hagberg, "Radiometric and interferometric calibration of ENVISAT-1 ASAR," Research Report No. 172, Department of Radio and Space Science, Chalmers University of Technology, Göteborg, (European Space Agency Contract Report: ASAR External Calibration and Validation Study, ESTEC Contract No. PO/133382), 1995.

[88] L. M. H. Ulander, "Radar remote sensing of sea ice: Measurements and theory," Ph.D. dissertation, Chalmers University of Technology, 1991.

[89] A. Freeman, "SAR calibration: an overview," *IEEE Transactions on Geoscience and Remote Sensing*, vol. 30, no. 6, pp. 1107–1121, 1992.

[90] M. Dobson, F. Ulaby, D. Brunfeldt, and D. Held, "External calibration of SIR-B imagery with area-extended and point targets," *IEEE Transactions on Geoscience and Remote Sensing*, vol. 24, no. 4, pp. 453–461, 1986.

[91] F. T. Ulaby, R. K. Moore, and A. K. Fung, *Microwave Remote Sensing, Active and Passive, Volume II: Radar Remote Sensing and Surface Scattering and Emission Theory*. Addison-Wesley, 1982.

[92] L. M. H. Ulander, "Radiometric slope correction of synthetic aperture radar images," *IEEE Transactions on Geoscience and Remote Sensing*, vol. 34, no. 5, pp. 1115–1122, 1996.

[93] O. Frey, M. Santoro, C. L. Werner, and U. Wegmuller, "DEM-Based SAR pixel-area estimation for enhanced geocoding refinement and radiometric normalization," *IEEE Geoscience and Remote Sensing Letters*, vol. 10, no. 1, pp. 48–52, 2013.

[94] E. P. W. Attema and F. T. Ulaby, "Vegetation modeled as a water cloud," *Radio Science*, vol. 13, no. 2, pp. 357–364, 1978.

[95] F. T. Ulaby, R. K. Moore, and A. K. Fung, *Microwave Remote Sensing, Active and Passive, Volume III: From Theory to Applications*. Addison-Wesley, 1988.

[96] J.-S. Lee and E. Pottier, *Polarimetric Radar Imaging: From Basics to Applications*. CRC Press, 2009.

[97] S. R. Cloude, *Polarisation Applications in Remote Sensing*. Oxford University Press, 2010.

[98] A. Reigber and A. Moreira, "First demonstration of airborne SAR tomography using multibaseline L-band data," *IEEE Transactions on Geoscience and Remote Sensing*, vol. 38, no. 5, pp. 2142–2152, 2000.

[99] S. R. Cloude, "Polarization coherence tomography," *Radio Science*, vol. 41, no. 4, pp. 1–27, 2006.

[100] S. Tebaldini, "Single and multipolarimetric SAR tomography of forested areas: A parametric approach," *IEEE Transactions on Geoscience and Remote Sensing*, vol. 48, no. 5, pp. 2375–2387, 2010.

[101] O. Ponce, P. Prats-Iraola, R. Scheiber, A. Reigber, A. Moreira, and E. Aguilera, "Polarimetric 3-D reconstruction from multicircular SAR at P-band," *IEEE Geoscience and Remote Sensing Letters*, vol. 11, no. 4, pp. 803–807, 2014.

[102] O. Ponce, P. Prats-Iraola, M. Pinheiro, M. Rodriguez-Cassola, R. Scheiber, A. Reigber, and A. Moreira, "Fully polarimetric high-resolution 3-D imaging with circular SAR at L-band," *Geoscience and Remote Sensing, IEEE Transactions on*, vol. 52, no. 6, pp. 3074–3090, 2014.

[103] F. T. Ulaby and C. Elachi, Eds., *Radar Polarimetry for Geoscience Applications*. Artech House, 1990.

[104] S. Cloude and E. Pottier, "An entropy based classification scheme for land applications of polarimetric SAR," *IEEE Transactions on Geoscience and Remote Sensing*, vol. 35, no. 1, pp. 68–78, 1997.

[105] A. Freeman and S. Durden, "A three-component scattering model for polarimetric SAR data," *IEEE Transaction on Geoscience and Remote Sensing*, vol. 36, no. 3, pp. 963–973, 1998.

[106] H. Zebker and J. Villasenor, "Decorrelation in interferometric radar echoes," *IEEE Transactions on Geoscience and Remote Sensing*, vol. 30, no. 5, pp. 950–959, 1992.

[107] E. Rodriguez and J. Martin, "Theory and design of interferometric synthetic aperture radars," *IEE Proceedings F Radar and Signal Processing*, vol. 139, no. 2, pp. 147–159, 1992.

[108] F. Gatelli, A. M. Guarnieri, F. Parizzi, P. Pasquali, C. Prati, and F. Rocca, "The wavenumber shift in SAR interferometry," *IEEE Transactions on Geoscience and Remote Sensing*, vol. 32, no. 4, pp. 855–865, 1994.

[109] S. Duque, U. Balss, C. Rossi, T. Fritz, and W. Balzer, "TanDEM-X payload ground segment, CoSSC generation and interferometric considerations," Remote Sensing Technology Institute, German Aerospace Center (DLR), Tech. Rep., 2012.

[110] J. O. Hagberg, L. M. H. Ulander, and J. I. H. Askne, "Repeat-pass SAR interferometry over forested terrain," *IEEE Transactions on Geoscience and Remote Sensing*, vol. 33, no. 2, pp. 331–340, 1995.

[111] J. O. Hagberg, "Repeat-pass satellite SAR interferometry," Chalmers University of Technology, Tech. Rep., 1995.

[112] Q. Lin, J. Vesecky, and H. Zebker, "New approaches in interferometric SAR data processing," *IEEE Transactions on Geoscience and Remote Sensing*, vol. 30, no. 3, pp. 560–567, 1992.

[113] R. Scheiber and A. Moreira, "Coregistration of interferometric SAR images using spectral diversity," *IEEE Transactions on Geoscience and Remote Sensing*, vol. 38, no. 5, pp. 2179–2191, 2000.

[114] L. C. Morena, K. V. James, and J. Beck, "An introduction to the RADARSAT-2 mission," *Canadian Journal of Remote Sensing*, vol. 30, no. 3, pp. 221–234, 2004.

[115] Y. Kankaku, Y. Osawa, S. Suzuki, and T. Watanabe, "The overview of the L-band SAR onboard ALOS-2," in *Progress in Electromagnetics Research Symposium*, Moscow, Russia, 18–21 August 2009, pp. 735–738.

[116] R. K. Arora, C. V. N. Rao, B. V. Bakori, R. Neelakantan, and J. G. Vachchani, "Synthetic aperture radar payload on-board RISAT-1: Configuration, technology and performance," *Current Science*, vol. 104, no. 4, pp. 447–461, 2013.

[117] R. Horn, "E-SAR – The experimental airborne L/C-band SAR system of DLR-HR," in *IEEE International Geoscience and Remote Sensing Symposium (IGARSS)*, Edinburgh, UK, September 12–16 1988, pp. 1025–1026.

[118] R. Horn, M. Werner, and B. Mayr, "Extension of the DLR airborne synthetic aperture radar, E-SAR, to X-band," in *IEEE International Geoscience and Remote Sensing Symposium (IGARSS)*, College Park, MA, USA, May 20–24 1990, pp. 2047–2047.

[119] R. Horn, "The DLR airborne SAR project E-SAR," in *IEEE International Geoscience and Remote Sensing Symposium (IGARSS)*, Lincoln, NE, USA, May 27–31 1996, pp. 1624–1628.

[120] I. Hajnsek, R. Scheiber, M. Keller, R. Horn, S. Lee, L. M. H. Ulander, A. Gustavsson, G. Sandberg, T. Le Toan, S. Tebaldini, A. M. Guarnieri, and F. Rocca, "BioSAR 2008 technical assistance for the development of airborne SAR and geophysical measurements during the BioSAR 2008 experiment: Final report – BioSAR campaign," ESA contract no. 22052/08/NL/CT, Tech. Rep., 2009.

[121] R. Horn, A. Nottensteiner, A. Reigber, J. Fischer, and R. Scheiber, "F-SAR: DLR's new multifrequency polarimetric airborne SAR," in *IEEE International Geoscience and Remote Sensing Symposium (IGARSS)*, Cape Town, South Africa, July 12–17 2009, pp. 902–905.

[122] F. Covello, F. Battazza, A. Coletta, E. Lopinto, C. Fiorentino, L. Pietranera, G. Valentini, and S. Zoffoli, "COSMO-SkyMed: An existing opportunity for observing the Earth," *Journal of Geodynamics*, vol. 49, no. 3, pp. 171–180, 2010.

[123] G. Triltzsch, "Challenges of automated processing of spaceborne high resolution SAR data," in *3rd International Asia-Pacific Conference on Synthetic Aperture Radar (APSAR)*, 2011, pp. 1–2.

[124] R. Torres, P. Snoeij, D. Geudtner, D. Bibby, M. Davidson, E. Attema, P. Potin, B. Rommen, N. Floury, and M. Brown, "GMES Sentinel-1 mission," *Remote Sensing of Environment*, vol. 120, pp. 9–24, 2012.

[125] X. Wang, G. Wang, Y. Guan, Q. Chen, and L. Gao, "Small satellite constellation for disaster monitoring in China," in *IEEE International Geoscience and Remote Sensing Symposium (IGARSS)*, Seoul, South Korea, July 25–29 2005, pp. 467–469.

[126] A. S. Gonzalez, M. Labriola, J. C. Soteras, and J. S. Palma, "PAZ instrument design and performance," in *3rd International Asia-Pacific Conference on Synthetic Aperture Radar (APSAR)*, Seoul, South Korea, September 26–30 2011, pp. 1–4.

[127] J. Janoth, S. Gantert, T. Schrage, and A. Kaptein, "From TerraSAR-X towards TerraSAR next generation," in *European Conference on Synthetic Aperture Radar (EUSAR)*, Berlin, Germany, June 3–5 2014, pp. 1337–1340.

[128] D. D'Aria, D. Giudici, A. M. Guarnieri, P. Rizzoli, and J. Medina, "A wide swath, full polarimetric, L band spaceborne SAR," in *IEEE Radar Conference*, Rome, Idaly, May 26–30 2008, pp. 1–4.

[129] J. Colinas, G. Séguin, and P. Plourde, "Radarsat Constellation, moving toward implementation," in *IEEE International Geoscience and Remote Sensing Symposium (IGARSS)*, Honolulu, HI, USA, 25–30 July 2010, pp. 3232–3235.

[130] M. Zink, M. Bachmann, B. Brautigam, T. Fritz, I. Hajnsek, A. Moreira, B. Wessel, and G. Krieger, "TanDEM-X: The new global DEM takes shape," *IEEE Geoscience and Remote Sensing Magazine*, vol. 2, no. 2, pp. 8–23, 2014.

[131] T.-D. Wu, K.-S. Chen, J. Shi, H.-W. Lee, and A. K. Fung, "A study of an AIEM model for bistatic scattering from randomly rough surfaces," *IEEE Transactions on Geoscience and Remote Sensing*, vol. 46, no. 9, pp. 2584–2598, 2008.

[132] F. T. Ulaby, K. Sarabandi, K. McDonald, M. Whitt, and M. C. Dobson, "Michigan microwave canopy scattering model (MIMICS)," University of Michigan, Tech. Rep., 1988.

[133] F. T. Ulaby, K. Sarabandi, K. McDonald, M. Whitt, and M. C. Dobson, "Michigan microwave canopy scattering model," *International Journal of Remote Sensing*, vol. 11, no. 7, pp. 1223–1253, 1990.

[134] G. Sun and K. J. Ranson, "A three-dimensional backscatter model of forest canopies," *IEEE Transactions on Geoscience and Remote Sensing*, vol. 33, no. 2, pp. 372–382, 1995.

[135] M. Moghaddam and S. Saatchi, "Analysis of scattering mechanisms in SAR imagery over boreal forest: Results from BOREAS '93," *IEEE Transactions on Geoscience and Remote Sensing*, vol. 33, no. 5, pp. 1290–1296, 1995.

[136] M. L. Williams, *PolSARproSim: A Coherent, Polarimetric SAR Simulation of Forests for PolSARPro; Design Document and Algorithm Specification (u1.0)*, 2006.

[137] S. V. Nghiem, S. H. Yueh, R. Kwok, and F. K. Li, "Symmetry properties in polarimetric remote sensing," *Radio Science*, vol. 27, no. 5, pp. 693–711, 1992.

[138] A. K. Fung and K. S. Chen, *Microwave Scattering and Emission Models for Users*. Artech House, 2010.

[139] M. A. Karam, A. K. Fung, and Y. M. M. Antar, "Electromagnetic wave scattering from some vegetation samples," *IEEE Transactions on Geoscience and Remote Sensing*, vol. 26, no. 6, pp. 799–808, 1988.

[140] Y.-C. Lin and K. Sarabandi, "Electromagnetic scattering model for a tree trunk above a tilted ground plane," *IEEE Transactions on Geoscience and Remote Sensing*, vol. 33, no. 4, pp. 1063–1070, 1995.

[141] J. Lopez-Sanchez, H. Esteban-Gonzalez, M. Baquero-Escudero, and J. Fortuny-Guasch, "An electromagnetic scattering model for multiple tree trunks above a tilted rough ground plane," *IEEE Transactions on Geoscience and Remote Sensing*, vol. 37, no. 2, pp. 659–667, 1999.

[142] M. Brolly and I. H. Woodhouse, "A matchstick model of microwave backscatter from a forest," *Ecological Modelling*, vol. 237–238, pp. 74–87, 2012.

[143] E. Blomberg, M. J. Soja, and L. M. H. Ulander, "P-band polarimetric model of vertical tree stems on sloping ground," in *IEEE International Geoscience and Remote Sensing Symposium (IGARSS)*, Quebec City, QC, Canada, July 13–18 2014, pp. 80–83.

[144] E. Rignot, J. Way, C. Williams, and L. Viereck, "Radar estimates of aboveground biomass in boreal forests of interior Alaska," *IEEE Transactions on Geoscience and Remote Sensing*, vol. 32, no. 5, pp. 1117–1124, 1994.

[145] R. Freedman, "Size and shape in biology," *Scientific American*, vol. 224, 1971.

[146] G. B. West, J. H. Brown, and B. J. Enquist, "A general model for the origin of allometric scaling laws in biology," *Science*, vol. 276, no. 5309, pp. 122–126, 1997.

[147] Y. Dong and J. Richards, "Studies of the cylinder-ground double bounce scattering mechanism in forest backscatter models," *IEEE Transactions on Geoscience and Remote Sensing*, vol. 33, no. 1, pp. 229–231, 1995.

[148] H. Israelsson, L. M. H. Ulander, T. Martin, and J. I. H. Askne, "A coherent scattering model to determine forest backscattering in the VHF-band," *IEEE*

Transactions on Geoscience and Remote Sensing, vol. 38, no. 1, pp. 238–248, 2000.

[149] B. Hallberg, G. Smith-Jonforsen, L. M. H. Ulander, and G. Sandberg, "A physical-optics model for double-bounce scattering from tree stems standing on an undulating ground surface," *IEEE Transactions on Geoscience and Remote Sensing*, vol. 46, no. 9, pp. 2607–2621, 2008.

[150] Y.-C. Lin and K. Sarabandi, "A Monte Carlo coherent scattering model for forest canopies using fractal-generated trees," *IEEE Transactions on Geoscience and Remote Sensing*, vol. 37, no. 1, pp. 440–451, 1999.

[151] Y.-C. Lin and K. Sarabandi, "Retrieval of forest parameters using a fractal-based coherent scattering model and a genetic algorithm," *IEEE Transactions on Geoscience and Remote Sensing*, vol. 37, no. 3, pp. 1415–1424, 1999.

[152] L. Thirion, E. Colin, and C. Dahon, "Capabilities of a forest coherent scattering model applied to radiometry, interferometry, and polarimetry at P- and L-band," *IEEE Transactions on Geoscience and Remote Sensing*, vol. 44, no. 4, pp. 849–862, 2006.

[153] M. A. Karam, A. K. Fung, R. H. Lang, and N. S. Chauhan, "A microwave scattering model for layered vegetation," *IEEE Transactions on Geoscience and Remote Sensing*, vol. 30, no. 4, pp. 767–784, 1992.

[154] C. C. Hsu, H. C. Han, R. T. Shin, J. A. Kong, A. Beaudoin, and T. Le Toan, "Radiative transfer theory for polarimetric remote sensing of pine forest at P band," *International Journal of Remote Sensing*, vol. 15, no. 14, pp. 2943–2954, 1994.

[155] M. L. Imhoff, "A theoretical analysis of the effect of forest structure on synthetic aperture radar backscatter and the remote sensing of biomass," *IEEE Transactions on Geoscience and Remote Sensing*, vol. 33, no. 2, pp. 341–352, 1995.

[156] G. Picard, T. Le Toan, S. Quegan, Y. Caraglio, and T. Castel, "Radiative transfer modeling of cross-polarized backscatter from a pine forest using the discrete ordinate and eigenvalue method," *IEEE Transactions on Geoscience and Remote Sensing*, vol. 42, no. 8, pp. 1720–1730, 2004.

[157] P. Liang, M. Moghaddam, L. Pierce, and R. Lucas, "Radar backscattering model for multilayer mixed-species forests," *IEEE Transactions on Geoscience and Remote Sensing*, vol. 43, no. 11, pp. 2612–2626, 2005.

[158] J. E. S. Fransson, G. Smith, J. I. H. Askne, and H. Olsson, "Stem volume estimation in boreal forests using ERS-1/2 coherence and SPOT XS optical data," *International Journal of Remote Sensing*, vol. 22, no. 14, pp. 2777–2791, 2001.

[159] M. Santoro, J. Askne, G. Smith, and J. Fransson, "Stem volume retrieval in boreal forests from ERS-1/2 interferometry," *Remote Sensing of Environment*, vol. 81, no. 1, pp. 19–35, 2002.

[160] M. Santoro, A. Shvidenko, I. McCallum, J. Askne, and C. Schmullius, "Properties of ERS-1/2 coherence in the Siberian boreal forest and implications for stem volume retrieval," *Remote Sensing of Environment*, vol. 106, no. 2, pp. 154–172, 2007.

[161] J. Askne and M. Santoro, *Recent Interferometry Applications in Topography and Astronomy*. Morn Hill, 2012, ch. Experiences in Boreal Forest Stem Volume Estimation from Multitemporal C-Band InSAR.

[162] M. Santoro, J. I. H. Askne, and P. Dammert, "Tree height influence on ERS interferometric phase in boreal forest," *IEEE Transactions on Geoscience and Remote Sensing*, vol. 43, no. 2, pp. 207–217, 2005.

[163] J. T. Pullianen, K. Heiska, J. Hyyppä, and M. T. Hallikainen, "Backscattering properties of boreal forests at the C- and X-band," *IEEE Transactions on Geoscience and Remote Sensing*, vol. 32, no. 8, pp. 1041–1050, 1994.

[164] R. N. Treuhaft, S. N. Madsen, M. Moghaddam, and J. J. van Zyl, "Vegetation characteristics and surface topography from interferometric radar," *Radio Science*, vol. 31, pp. 1449–1485, 1996.

[165] J. Praks, F. Kugler, K. P. Papathanassiou, I. Hajnsek, and M. T. Hallikainen, "Height estimation of boreal forest: Interferometric model-based inversion at L- and X-band versus HUTSCAT profiling scatterometer," *IEEE Geoscience and Remote Sensing Letters*, vol. 4, no. 3, pp. 466–470, 2007.

[166] S. R. Cloude, "Dual-baseline coherence tomography," *IEEE Geoscience and Remote Sensing Letters*, vol. 4, no. 1, pp. 127–131, 2007.

[167] M. Lavalle, M. Simard, and S. Hensley, "A temporal decorrelation model for polarimetric radar interferometers," *IEEE Transactions on Geoscience and Remote Sensing*, vol. 50, no. 7, pp. 2880–2888, 2012.

[168] L. G. Marklund, "Biomassafunktioner för tall, gran och björk i Sverige," Institutionen för skogstaxering, Sveriges lantbruksuniversitet, Umeå, Sweden, Rapport 45, 1988.

[169] H. Petersson, "Biomassafunktioner for trädfraktioner av tall, gran och björk i sverige," SLU, Institutionen för skoglig resurshållning och geomatik, Arbetsrapport 59, Umeå, Tech. Rep., 1999, (in Swedish).

[170] P. Wikström, L. Edenius, B. Elfving, L. O. Eriksson, T. Lämäs, J. Sonesson, K. Öhman, J. Wallerman, C. Waller, and F. Klintebäck, "The Heureka

forestry decision support system: An overview," *Mathematical and Computational Forestry & Natural-Resource Sciences*, vol. 3, no. 2, pp. 87–94, 2011.

[171] M. J. Soja, "Modelling and retrieval of forest parameters from synthetic aperture radar data," Chalmers University of Technology, Tech. Rep., 2012.

[172] S. Solberg, R. Astrup, J. Breidenbach, B. Nilsen, and D. Weydahl, "Monitoring spruce volume and biomass with InSAR data from TanDEM-X," *Remote Sensing of Environment*, vol. 139, pp. 60–67, 2013.